2007

Hardware Implementation of Active Disturbance Rejection Control for Vibrating Beam Gyroscope

David Avanesian
Cleveland State University

HARDWARE IMPLEMENTATION OF ACTIVE DISTURBANCE REJECTION CONTROL FOR VIBRATING BEAM GYROSCOPE

DAVID AVANESIAN

Bachelor of Electrical Engineering

Cleveland State University

May, 2006

submitted in partial fulfillment of requirements for the degree

MASTER OF SCIENCE IN ELECTRICAL ENGINEERING

at the

CLEVELAND STATE UNIVERSITY

December, 2007

This thesis has been approved
for the Department of Electrical and Computer Engineering
and the College of Graduate Studies by

_____

Thesis Committee Chairperson, Lili Dong

_____

Department/Date

_____

Dr. Dan Simon

_____

Department/Date

_____

Dr. Zhiqiang Gao

_____

Department/Date

_____

Dr. George L. Kramerich

_____

Department/Date

ACKNOWLEDGEMENTS

I would like to thank my advisor Dr. Lili Dong, for constant support and help.

I would like to thank committee members Dr. Gao and Dr. Simon for their support and guidance. I am very appreciative for Dr. Gao giving me an opportunity to work in the Center of Advanced Control Technologies that helped me to obtain a great deal of experience.

Special thanks go to Dr. Kramerich for constant support, guidance and monitoring my progress. I am very appreciative of your constant involvement and interest in my research.

I would like to thank my colleagues Harry Olar, Anthony Roberts, Joe Rymut, and Qing Zheng for constant support and friendship.

Special thanks go to Daniel and Jamie Raible for unconditional support, guidance, friendship and help. I really appreciate your constant involvement and interest in my work and thank you for teaching me things that were very new to me.

Special thanks and appreciation go to my family and friends for their constant moral and physical support, appreciation for what I do, involvement and help. Special thanks to my brother Tigran and a good friend Greg for constant moral support.

My deepest appreciation goes to my grandmother Issabella for making me a better person and making me believe that everything is possible.

HARDWARE IMPLEMENTATION OF ACTIVE DISTURBANCE REJECTION CONTROL FOR VIBRATING BEAM GYROSCOPE

DAVID AVANESIAN

ABSTRACT

Obtaining the approximation of rotation rate form a Z-Axis MEMS gyroscope is a challenging problem. Currently, most commercially available MEMS gyroscopes are operating in an open-loop for purposes of simplicity and cost reduction. However, MEMS gyroscopes are still fairly expensive and are not robust during operation.

The purpose of this research was to develop a high-performance and low-cost MEMS gyroscope using analog Active Disturbance Rejection Control (ADRC) system. By designing and implementing analog ADRC both above requirements were satisfied. Analog ADRC provides the fastest response time possible (because the circuit is analog), eliminates both internal and external disturbances, and increases the bandwidth of the gyroscope beyond its natural frequency. On the other hand, the overall design is extremely economical, given that the system is built using pure active and passive analog components.

This work, besides achieving high-performance and providing low-cost solution, furnishes two novel designs concepts. First, Active Disturbance Rejection Controller can now be build using pure analog circuit, which has never been done before. Second, it is the first time that the advanced controller has been successfully implemented in hardware to control an inertial rate sensor like gyroscope. This work provides a novel solution to applications that require high-performance and low-cost inertial sensors.

TABLE OF CONTENTS

Page

NOMENCLATURE

ADRC: Active Disturbance Rejection Control

MEMS: Micro-Electromechanical System

VBG: Vibrating Beam Gyroscope

FPAA: Field Programmable Analog Array

Op-Amp: Operation Amplifier

LPF: Low-Pass Filter

HPF: High-Pass Filter

BPF: Band-Pass Filter

ESO: Extended State Observer

LIST OF TABLES

Table **Page**

LIST OF FIGURES

Figure **Page**

CHAPTER I

INTRODUCTION

In 1817 mathematician Johann Bohnenberger created world's first mechanical gyroscope and called it "Machine". The device was introduced to French mathematician Pierre-Simon Laplace, who suggested using the gyroscope as an educational tool.

Figure 1: First Gyroscope

In 1852 French mathematician Leon Foucault used the "Machine" for an experiment involving rotation rate of Earth. Even though the experiment was unsuccessful, the name "gyroscope" came out of it ("gyros" for *rotation* and "skopeein" for *see*).

The gyroscope became extremely useful when it was combined with an electric motor to make a prototype of first gyrocompasses. First functional gyrocompass was created by a German inventor Hermann Anschultz-Kaemmpfe from 1905 to 1908. In the time when naval industry was the measure of power, many countries realized the importance and contribution of gyroscopes to naval and aircraft stabilization and control. In 1910, American inventor Elmer Sperry created his own gyroscope design, which became the first product for the Sperry Gyroscope Company. The design was so popular that it became a major factor in naval and aircraft research and development.

With major development in micro-systems and microelectronics in the past 40 to 50 years, the traditional mechanical gyroscopes are being rapidly replaced with Micro-Electromechanical Gyroscopes (MEMS Gyroscopes). Systron Donner Inertial (SDI) was the first company to produce fully functional MEMS Gyroscopes and is one of the largest manufacturers up to date. Although, the MEMS Gyroscopes have many advantages over their predecessors, they have their own issues. This work addresses and solves some of the problems that MEMS industry is facing.

1.1 Background

Since the development of a first MEMS device, MEMS industry has seen a huge progress. With MEMS devices becoming more versatile, higher performance and batch fabricated, the amount of applications increased exponentially. The MEMS pressure

sensor has the highest sales volume in the past 15 years, with MEMS accelerometer being the second largest. Some of the reasons for such popularity for these devices are innovations in micro-fabrication and low cost due to batch fabrication.

The rapid progress in silicon-based micro-machining started in early 60's, when Integrated Circuits (IC) technology process was created. With strong effort being centered on silicon etching and chemical deposition research, first commercially available micro-fabricated pressure sensor was created by 1980's. Improvement in those processes and better understanding of electrical and mechanical properties of materials, led to integration of micro-machining (mechanical structure) and IC technology (electrical circuit). In the beginning of 1990's, complex Micro-Electromechanical Systems (MEMS) were fully developed that included sensors, actuators and supporting electronics on the same silicon wafer.

Although the MEMS devices offer many advantages and are increasingly used in different applications, they had and still have performance issues. In early 80's those issues were understood to be due to imperfections during fabrication. Mechanical and thermal noise issues led to research in material science to improve thermal stability. Unknown system parameters, asymmetric damping and spring coupling and small operation bandwidth led to search in improvement in fabrication process steps. In the past 15 to 20 years, most of the research was focused on improving MEMS fabrication to achieve higher performance systems. The aftermath of this research was creation of two main types of micro-machining (surface and bulk micro-machining), generation of fabrication process steps foundries (PolyMUMPS, SUMMIT V), numerous actuation and

sensing mechanisms (Electro-Static, Piezoelectric, Comb Drive) and different design styles for different devices.

However, improvement in performance increased the cost of micro-fabrication of MEMS devices. Tight tolerances, expensive equipment and facilities are main factors for cost per device still being relatively high. Companies that were involved in producing accelerometers and pressure sensors realized that increase in a market share could only occur if they can offer not only high performance, but low-cost MEMS devices as well. They were able to achieve market's price target by investing in new generations of MEMS sensors that broke the price barrier. Unlike MEMS accelerometers and pressure sensors, MEMS gyroscope industry is still struggling with high cost issue. There are only a few high performance MEMS gyroscopes on the market, but they are still relatively costly for many applications. At this point, only military and high end automotive applications can afford MEMS gyroscopes, since the cost for these applications is not a prime concern.

Most of the problems that are listed above understood to be due to imperfections in micro-fabrication or in design styles that are currently used. So far, most of the researchers focus on improving micro-fabrication to obtain higher performance sensors and try to drive cost down. However, this perception is changing towards employing closed loop control system. In [1] Adaptive add-on controller is used to control conventional mode of operation of MEMS gyroscope. The controller is an addition to force-balancing scheme for parameter estimation. The algorithm approximates the angular rate and compensates the quadrature error. The main point of using adaptive controller is to obtain angular rate without quadrature error contamination. Adaptive

controller gives positive simulation results, but it is model dependant and no hardware implementation has yet been done. Controllers such as Kalman filter in [2] and other force-balancing controllers in [3] and [4] increased the operational bandwidth of the system, but those two methods are still model dependant and performance will degrade with parameter variations. In [5], feedback control is used to control piezoelectric resonator that is used in MEMS gyroscopes. The closed loop control system replaces the traditional mechanical balancing operation. Controller adjusts the resonant frequency and increases the bandwidth of operation. However, the method does not include constant amplitude of oscillations and is not involved in rotation rate measurement. In [6], dual stage control architecture is used to correct the manufacturing imperfections. The controller includes calibration and feedback capabilities. Calibration portion of a controller tries to eliminate large imperfection, while feedback portion is dealing with remaining small non-linearity. However, ideal gyroscope model is used without taking non-linearity's and couplings into account and no hardware results are presented. Another example of using an adaptive controller is presented in [7]. The adaptive controller is a discrete observer-based adaptive controller that approximates rotation rate and tries to deal with mechanical imperfections. Like in many other applications of adaptive controllers on MEMS gyroscope, precise mathematical model is required for the controller to work. Also, the mathematics behind the development of a controller is quite complex, and using digital computers is certainly an option, but the implementation will be computationally intensive, which will most definitely increase the overall cost of the device. An interesting idea was proposed in [8], where gyroscope is designed using two vibrating masses instead of one. The authors claim that such design will increase the

operating bandwidth of the gyroscope without using advanced control electronics. Also, tight tolerance requirements might not be needed anymore due to advantages listed above. However, constructing two masses instead of one could potentially give two times more uncertainties and cost might either stay the same or increase. Although advanced controller might not be required, some other simpler controller strategy will have to be implemented, since the oscillation amplitude for a second mass must remain constant for the system to work. Also, no experimental results have backed up the proposed theory. The control approach in [9] shows both non-adaptive and adaptive strategies using active non-linear feedback. The work is basically a summary of principles of operation of a gyroscope and general formulation of control problems with it. However, the methodology heavily depends on modeling of the system and no experimental results are given.

The above given references show that the MEMS gyroscope industry is shifting towards employing closed-loop control strategies in order to improve the performance of the system. Although there are many publications that use many different closed-loop control methods, they are either model dependant, hard to implement due to computation intensity or expensive. It is clear that by improving micro-fabrication only, it is impossible to design high performance and low cost systems at the same time. By adding closed loop controller to the system we can allow imperfections to occur during micro-fabrication. In addition, any unknown disturbances (external and/or internal) can be reduced or eliminated by using a closed loop controller. With control system the micro-fabrication process does not have to have such tight tolerances during fabrication process and that will allow more flexibility in design process and will result in a cost reduction.

Currently, supporting electronics that is packaged together with a mechanical structure is generally used for signal conditioning and user interface. Therefore, MEMS gyroscopes that are currently used in 90% of industry are generally operating in either open loop, pre-shaped open-loop driving or employ very simple control structures like PLL and AGC. Main reason for choosing those types of operation versus closed loop is simplicity on a design and operation levels.

This thesis tries to accommodate deficiencies of above referenced work and industry needs to design higher performance/low-cost MEMS gyroscope sensor. By doing so, we came up with a completely novel control concept that solves all of the problems of other controllers, increases performance of a given gyroscope and decreases the cost of the overall system. We use Active Disturbance Rejection Control (ADRC) [12, 13, 14, 15, 16, 17, 18, 19, 20, 21, and 22] methodology to control the device as well as approximate rotation rate. The main difference between ADRC and other advanced controllers is that it does not require precise mathematical model of a plant to be able to successfully control it. Instead of using precise mathematical model, ADRC contains Extended State Observer (ESO), which precisely tracks internal and external disturbances of the plant and cancels them in a real time. The only plant information that ADRC requires is the relative order of the plant and its bandwidth. Using this information ESO approximates state of the plant and generalized disturbance of the system. Approximated disturbance is then canceled and system becomes a double integral plant that can be easily controlled with a PD controller. ADRC algorithm is inherently scalable and can be utilized to solve many different control problems. If this capability is realized in hardware implementation, many control problems can be rapidly addressed without tedious

redesign process. Versatility of ADRC has been demonstrated on problems such as motion control, jet engine control, power electronics, satellite attitude control, magnetic bearings, and human posture sway. Each of these problems varies in complexity, requiring different variations of the base algorithm and different methods of implementation.

The most common method of implementing ADRC is with general purpose sequential processors. This includes the use of microcontrollers, digital signal processors (DSPs) and field programmable gate arrays (FPGAs) with embedded microprocessors. Generally, digital implementation provides scalability and repeatability, but may also be expensive. Depending on the application, the response time of the digital controller may degrade the performance of the overall system.

In our design we chose not to use digital implementation for controlling of MEMS gyroscope. We chose to design and build ADRC using pure analog implementation, which has never been done before. Analog implementation gives us several advantages over its digital counterpart. First, MEMS gyroscope sensor needs to have the fastest response time possible to ensure high performance and analog circuit is the fastest hardware implementation method, since it is instantaneous. Secondly, analog implementation of ADRC is very economical comparing to a digital implementation of previously designed ADRC topology for other applications. Third, the designed analog circuit is power efficient and small, which is very important in MEMS industry. The disadvantage of using analog circuit versus digital is that it is not easily scalable. For example, if the order of a plant increases the existing controller will not work without adding hardware to accommodate the increase in plant order. However, the purpose of

this work was to find an efficient, high performance and economical solution for improving MEMS gyroscope sensor. MEMS gyroscope industry is extremely broad and it is simply impossible to design a system that would suit all applications. And our design is not an exception. Analog ADRC for MEMS gyroscope design is particularly good for specific applications with specific problems, and it solves them very well. Such specific problems are high performance issues, cost per device, response time, bandwidth of operation and general disturbances.

In the next subsections we will describe the general applications of MEMS gyroscopes, top level hierarchy of a controller and general outline of the thesis.

1.2 Application in Industry

There are three main applications where MEMS devices, particularly MEMS gyroscopes, are used. First and the fastest growing application is automotive. MEMS gyroscopes are used for anti rollover system, GPS navigation and electronic stability control.

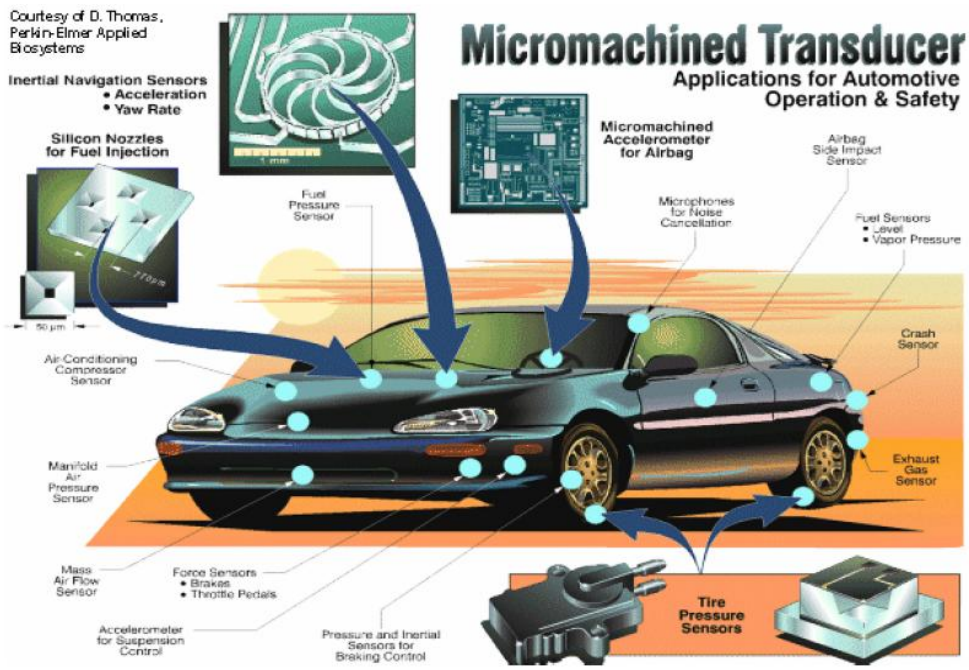

Figure 2: Automotive Application

Cost of a gyroscope still remains the biggest problem car manufacturer's face today. Only high end cars can afford implementation of MEMS gyroscopes.

Military is the second largest application of MEMS gyroscopes. It includes navigation, flight control, platform stabilization, missile guidance, and etcetera.

Figure 3: Military Application

In military application the most important system parameter is its performance. Generally, MEMS gyroscopes used in military application are expensive. The high cost is driven by a need of high performance and tight tolerances. Such gyroscopes are application specific and would rarely be employed in other applications.

Third main MEMS gyroscopes application is consumer electronics. Gyroscopes are used in camcorder stabilization, camera stabilization, cell phone stabilization, video games, digital light processing and many others.

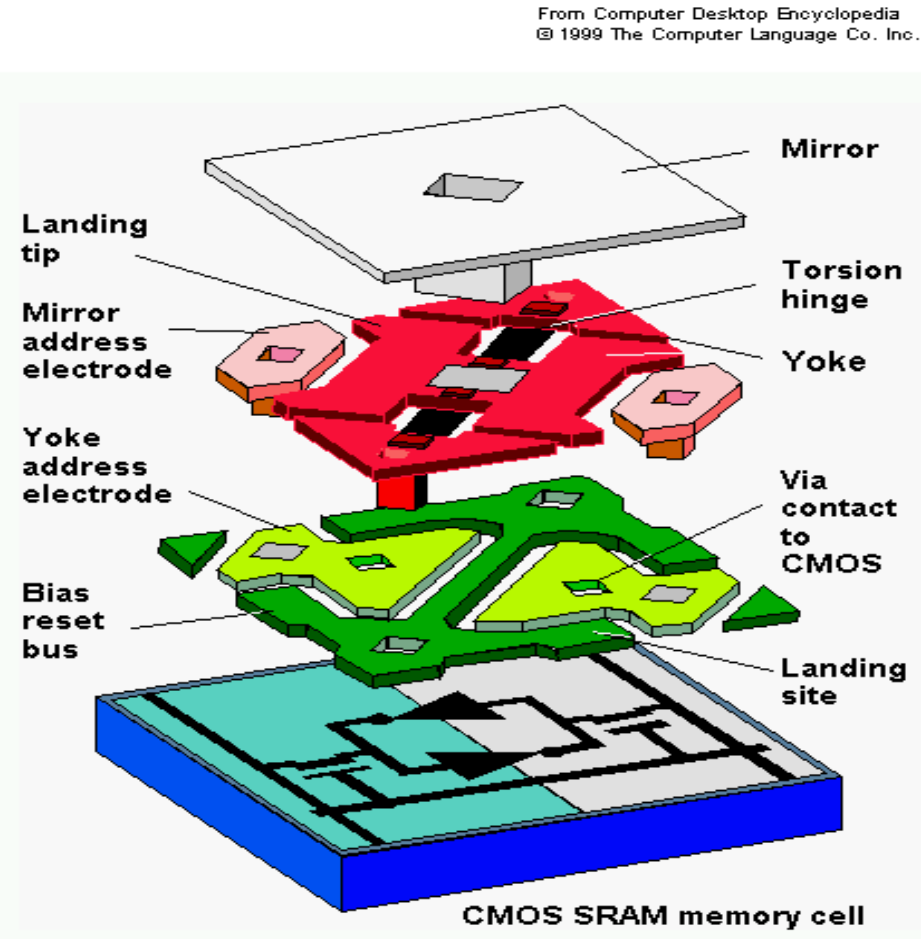

Figure 4: Consumer Application

The main challenge of employing gyroscopes for consumer electronics is cost of a sensor. Most of the devices that use MEMS gyroscopes are still expensive and consider being high end products. Driving cost of MEMS gyroscopes has become the most important task for MEMS manufacturers and researchers in the area. Achieving the market requirement for low-cost MEMS gyroscopes is essential. Once the market's price target is met, the MEMS gyroscopes industry will see drastic increase in sales volume.

1.3 Problem Formulation

Most MEMS Gyroscopes use vibrating mechanical element or proof mass to sense rotation. This approach eliminates rotating parts, which leads to small size device that can be easily batch fabricated using micro-machining techniques. MEMS gyroscope is understood as a proof mass that is attached to a fixed frame by means of springs and dampers.

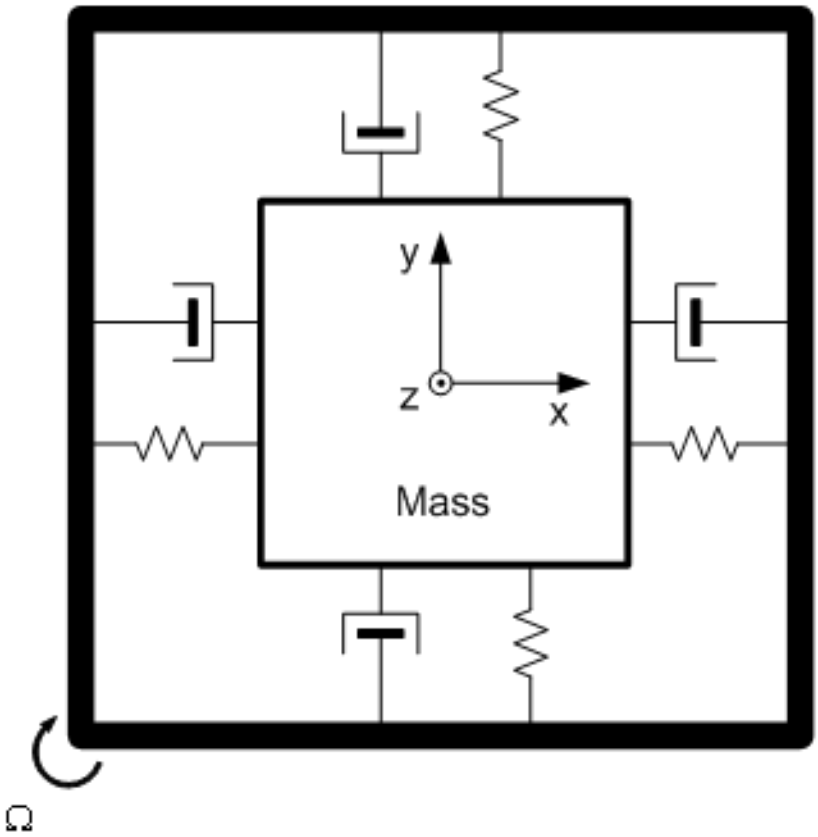

Figure 5: Model of a MEMS Gyroscope

The horizontal axis (denoted x) is called Drive Axis and vertical axis (denoted y) is called Sense Axis. The axis that is perpendicular to both Drive and Sense axis (denoted

z) is called Z axis or rotation axis. Drive and Sense axis can be represented as second order coupled systems:

$$m\ddot{x} + d_{xx}\dot{x} + k_{xx}x - m\Omega_z^2 x + k_{xy}\dot{y} - m\dot{\Omega}_z y - 2m\Omega_z \dot{y} = u_{drive} \quad (1)$$

$$m\ddot{y} + d_{yy}\dot{y} + k_{yy}y - m\Omega_z^2 y + k_{xy}x + d_{xy}\dot{x} + m\dot{\Omega}_z x + 2m\Omega\dot{x} = u_{sense} \quad (2)$$

Where x, y are displacement output of drive and sense axis. $d_{xx}\dot{x}, d_{yy}\dot{y}$ are damping terms of drive and sense axis. $K_{xx}x, K_{yy}y$ are spring forces along drive and sense axis. $d_{xy}\dot{x}, d_{xy}\dot{y}$ are asymmetric damping coupling terms caused by fabrication imperfections. $K_{xy}x, K_{xy}y$ are asymmetric spring coupling terms caused by fabrication imperfections. $m\Omega_z^2 x, m\Omega_z^2 y$ are centrifugal forces along X and Y axis. $2m\Omega_z\dot{x}, 2m\Omega_z\dot{y}$ are Coriolis forces along drive and sense axis. Equations (1) and (2) represent full mathematical model for MEMS gyroscope. In our design we make the following assumptions: Rotation rate is constant, damping coupling terms are zero, and centrifugal forces are zero. The mathematical model for MEMS gyroscope becomes:

$$\ddot{x} + \frac{\omega_x}{Q_x}\dot{x} + \omega_x^2 x + \omega_{xy} y - 2\Omega\dot{y} = \frac{1}{m}u_{drive} \quad (3)$$

$$\ddot{y} + \frac{\omega_y}{Q_y}\dot{y} + \omega_y^2 y + \omega_{xy} x + 2\Omega\dot{x} = \frac{1}{m}u_{sense} \quad (4)$$

Where $\frac{\omega_x}{Q_x} = \frac{d_{xx}}{m} = 2\xi_x, \quad \omega_n^2 = \frac{k_{xx}}{m}, \quad \omega_{xy} = \frac{k_{xy}}{m}, \quad \frac{\omega_y}{Q_y} = \frac{d_{yy}}{m} = 2\xi_y, \quad \omega_y^2 = \frac{k_{yy}}{m}$

Equations (3) and (4) are coupled second order representation of Drive and Sense axis. Quality factor (Q) of both axis is generally very large number, therefore the

damping coefficient ($\xi = \frac{1}{2Q}$) is very small. This feature of MEMS gyroscopes makes them lightly damped second order systems that have a very sharp resonant peak.

All vibratory gyroscopes are based on transfer energy between two vibrating axis of a structure caused by Coriolis acceleration. Electrostatic actuators force the motion of the mass in one direction (drive). When the sensor is rotated around Z-Axis, the mass experiences the Coriolis force F:

$$F(t) = -2m\Omega_z(t) \times \dot{x}(t) \tag{5}$$

where m is a proof mass, Ω_z is angular velocity and $\dot{x}$ is the velocity of the proof mass. The equation (5) contains vector product, since proof mass velocity and angular velocity are both vectors. The drive, sense and z axis are all orthogonal to each other and, therefore, the Coriolis acceleration ($a(t) = -2\Omega_z(t)\dot{x}(t)$) acts along sense axis. During implementation, proof mass velocity is a sinusoid with a constant frequency. Generally, frequency of this sinusoid is a lot larger then the frequency of the angular velocity signal. As a result, Coriolis acceleration can be represented as a double-sideband modulated signal, where the proof mass velocity is a carrier and angular velocity is the information carrying signal. Therefore, in order to retrieve the rotation rate information, Coriolis acceleration must be sensed and demodulated.

In our design we make three requirements for MEMS gyroscope to operate properly. First, the rigid frame must be rotating at a constant rate Ω. Second, drive axis must be driven to resonance, in order to obtain the maximum amplitude. Third, we use force-to-rebalance control on sense axis, where the output is monitored in real time and forced to zero. With output of sense axis being zero, control signal of sense axis becomes

the rotation rate information carrying signal. As mentioned above, we will use demodulation techniques to obtain rotation rate.

In the following subsections we will describe each requirement on details.

1.3.1 Drive Axis Control

As mentioned above, drive axis of a MEMS gyroscope is a represented as a second order lightly damped system. Its large quality factor creates very sharp resonant characteristics with natural resonant frequency being in the range of 10-30 kHz. With MEMS gyroscope size being on a micrometer scale, all of the input and output signals are very small in magnitude. Most of the time it is pretty much impossible to distinguish the information carrying voltage signal from low voltage noise signals that are always present in a system. In order to separate drive axis output signal from noise, drive axis must be driven to resonance, where it has the highest amplitude. Given that drive axis has very large quality factor, it will have a very narrow and sharp resonant peak. The edge of the peak is generally 30 to 50 dB higher then the base amplitude of the signal. Basically, resonant peak acts as a natural amplifier and assuming the base amplitude is in micro-volts, if the drive axis operates at resonance the sensed voltage amplitude is generally in hundreds of milli-volts. Drive axis signal is a very important signal for approximating rotation rate. Equation (5) represents Coriolis force that contains rotation rate and velocity of the drive axis signals. If we do not operate drive axis at resonance we will not be able to obtain large enough Coriolis force and, therefore, will not be able to approximate rotation rate.

Most MEMS gyroscopes in industry use electrostatic actuators to force drive axis into resonant oscillations. However this method is an open-loop technique and has several issues. The oscillations of drive axis have uncontrolled amplitude and frequency (mainly due to temperature variations), which create large performance drifts. Uncontrolled amplitude creates drifts in Coriolis force, which in turn accumulates in a rotation rate approximation error. Since the resonant peak of drive axis is extremely narrow (generally a few Hertz) it is vital to have oscillations precisely at the natural frequency of the system. With temperature variations and other external disturbances keeping drive axis at resonance is a tough task if uncontrolled method is used, which results in heavy degrade in performance up to device loosing its sensitivity completely.

We use ADRC methodology to achieve the following goals: Obtain stable oscillations with constant frequency and amplitude and increase the bandwidth of the resonant peak of the drive axis. Constant amplitude will ensure zero drift in the approximated rotation rate. Constant frequency of oscillations will ensure stability during operation. Large system bandwidth will allow imperfections during micro-fabrication process, which will decrease the cost of the overall system.

1.3.2 Sense Axis Control

Model of a sense axis is generally the same as drive axis. It is represented using second order lightly damped resonant system. Most of the research has been focused on fabrication of sense axis that is perfectly aligned with drive axis (zero coupling terms). If we assume perfectly decoupled system, then we can force sense axis to resonant

oscillations, approximate Coriolis force (it acts along sense axis as it was mentioned above) and use simple demodulation technique to retrieve rotation rate. Nevertheless, mechanical imperfections always occur and they will create couplings between drive and sense axis. One way to eliminate coupling term is to mathematically model it as precisely as possible and then use control methodology to minimize its effect on the system's response. Although this method is one of the most popular ones among many researchers, we will use Force-to-Rebalance control method.

The idea behind Force-to-Rebalance method is to use a control algorithm (such as ADRC) to force the output of the system (sense axis) to zero. Nulling output of sense axis using ADRC methodology gives us several advantages. First, it eliminates the need to fabricate perfectly aligned dual axis system, which will greatly reduce the cost of the device. Secondly, instead of modeling dual axis couplings, we use its property to approximate the rotation rate.

Equation (4) represents second order sense axis system. Let's assume that force-to-rebalance method is successfully implemented and output of sense axis (y) is zero:

$$y = 0 \tag{6}$$

which means that any order of derivative of y will also be zero:

$$\dot{y} = \ddot{y} = 0 \tag{7}$$

Therefore equation (4) becomes:

$$\omega_{xy} x + 2\Omega\dot{x} = u_{sense} \tag{8}$$

Equation (8) contains a coupling term, Coriolis acceleration and control signal of sense axis. Assuming that drive axis output (x) is driven to resonance and oscillates with constant amplitude and frequency, control signal of sense axis is now rotation rate information carrying signal. By detecting control signal of sense axis and applying simple demodulation techniques and some other signal conditioning, we can extract the rotation rate information.

Successful implementation of ADRC to null the output of sense axis is essential for rotation rate approximation. Next subsection uses implementation of ADRC on both drive and sense axis to approximate rotation rate.

1.3.3 Rotation Rate Approximation

Although the control system design for drive and sense axis is essential for the system to perform, the ultimate goal of this project is to obtain correct rotation rate. We will approximate rotation rate using equation (8) with assumption that drive axis is oscillating at resonance and sense axis output is nulled.

Note that coupling term $\omega_{xy}x$ and Coriolis acceleration $2\Omega\dot{x}$ are 90^0 out of phase with each other. The goal here is to eliminate the coupling term and extract rotation rate (Ω) from Coriolis acceleration term. We will apply synchronous demodulation to control signal of sense axis, which is simply multiplying control signal (u_{sense}) by drive axis output (x):

$$x \cdot u_{sense} = x(\omega_{xy}x + 2\Omega\dot{x}) \tag{9}$$

In actual implementation, output of drive axis (x) is a sinusoidal function with fixed amplitude and frequency. The first derivative of x is also a sinusoidal function with fixed frequency and amplitude:

$$x = A\cos(\omega_x t), \quad \dot{x} = A\omega_x \sin(\omega_x t) \tag{10}$$

Applying equation (9) we get:

$$xu_{sense} = \omega_{xy} A\sin(\omega_x t)\cos(\omega_x t) - 2\Omega A\sin^2(\omega_x t) \tag{11}$$

$$xu_{sense} = \frac{1}{2}\omega_{xy} A\sin(2\omega_x t) - 2\Omega A\omega_x \frac{1-\cos(2\omega_x t)}{2} \tag{12}$$

$$xu_{sense} = \frac{1}{2}\omega_{xy} A\sin(2\omega_x t) + \Omega A\omega_x \cos(2\omega_x t) - \Omega A\omega_x \tag{13}$$

Equation (13) contains two parameters that have double frequency component and offset rotation rate Ω . The last step in rotation rate approximation is to apply a low-pass filter in order to filter out double frequency components, which will leave us with just rotation rate Ω and offset $A\omega_x$. After applying simple signal conditioning we obtain the rotation rate Ω .

1.4 Thesis Organization

In this thesis, in depth Active Disturbance Rejection Control design is proposed in Chapter 2. The design includes derivation of transfer function ADRC for analog

implementation. Extended State Observer algorithm is derived and necessary filter tuning is shown. Rotation Rate Approximation algorithm is derived and verified.

Chapter 3 contains all of the simulation results. At first, in depth Matlab simulation of ADRC on VBG is shown. Then, circuit simulation of ADRC on VBG is shown using LTSpice.

Chapter 4 contains all of the experimental results. Experimental set-up using high-performance turn table, analog circuit implementation for driving mode, sensing mode and demodulation with signal conditioning.

Finally, Chapter 6 offers concluding remarks about the impact and significance of this work and proposes possible future work.

CHAPTER II

ADAVANCED CONTROLLER DESIGN

This chapter will introduce the design of Active Disturbance Rejection Control. ADRC is a powerful control methodology that has had many successful applications already. The range of applications mentioned in Introduction is very broad, which means that the control methodology is very scalable and easily applicable to many different control problems. However, ADRC should not be understood as an equation or a formula. It must be understood as an idea that can be reformulated to fit a specific issue and be able to solve it. Depending on the application, equations that describe ADRC might very well be different, but the top-level idea always stays the same. Many applications up to date required digital implementation of ADRC. Different discretization techniques were used to describe particular ADRC equations in order to be able to use microcontrollers, digital signal processors (DSPs) and field programmable gate arrays (FPGAs) with embedded microprocessors. Digital implementation of ADRC has been very successful due to its scalability, repeatability and easy reconfiguration. But it also has some potential disadvantages, such as development time and cost. Development of ADRC using FPGA is a very rewarding process, but complex, time consuming and expensive. Using

sequential processors is cheaper, but complexity and time are generally the same as with using FPGAs. With an application like MEMS gyroscope, digital implementation could only work if the gyroscope is applied to a military system or high end automotive application because the cost and development time are not the issue. Since one of the goals of this work is to deliver a low cost MEMS gyroscope, digital implementation will not be suitable in this case.

Instead of using digital implementation, we reformulated ADRC to be represented in a transfer function form. Transfer function can be understood as a filter, poles and zeros of which are the cutoff frequencies. ADRC in transfer function form is a combination of different types of filters, which can be implemented using analog circuitry. Analog implementation of ADRC is a lot cheaper then the digital implementation and requires less development time. It can be build using active and passive components such as operational amplifiers, resistors and capacitors. The components are readily available at very low cost, which in turn reduces the cost of the overall system. The development time is reduced because there are many different known filter topologies well documented. Therefore, the redesign of a certain topology to fit the specific application is not a time consuming process. ADRC in analog form delivers high performance, robust and low cost system that can be used many applications that require these particular specifications. It the first time that ADRC is reformulated in transfer function form and successfully implemented in hardware. Analog implementation provides a good alternative to digital implementation of ADRC. Having both analog and digital ways of implementing ADRC the range of control applications is increased substantially.

2.1 Analog ADRC

Implementation of Active Disturbance Rejection Controller in analog form requires that the controller is represented in a transfer function form. Unlike state-space representation, transfer function from gives unique insights on frequency domain of the system. As mentioned above, control system can be understood as a certain combination of different types of filters. The combination of filters working together will shape up the required transient response (derivative or high-pass/band-pass filters); eliminate the steady-state error (integrator or low-pass filter), reject the high frequency disturbances and noises and will increase the operational bandwidth of the system beyond its limitations. In order to be able to analyze and design these filters, frequency domain analysis is essential. Using transfer function representation is the most straightforward way to analyze a system in a frequency domain. Frequency response analysis provides important information on gain and phase margins, stability and operational bandwidth.

In our case, the system consists of two identical second order systems (drive and sense axis). Therefore, we will only show the design of ADRC in transfer function form for drive axis with an assumption that the same procedure is used for sense axis. Consider the mathematical representation of drive axis (3):

$$\ddot{x} + \frac{\omega_x}{Q_x}\dot{x} + \omega_x^2 x + \omega_{xy} y - 2\Omega\dot{y} = \frac{1}{m}u_{drive} \tag{14}$$

$$\ddot{x} = -\frac{\omega_x}{Q_x}\dot{x} - \omega_x^2 x - \omega_{xy} y + 2\Omega\dot{y} + bu_{drive} \tag{15}$$

Where $b = \frac{1}{m}$. Equation (15) can be represented in a different form:

$$\ddot{x} = f(x, \dot{x}, w, t) + bu_{drive} \tag{16}$$

Where $f(x, \dot{x}, w, t)$ is a generalized disturbance function that represents all of the internal and external disturbances. From now on, for simplicity, we will denote this function just f. The idea behind this representation is that if generalized disturbance term is canceled, the overall system becomes a double integral plant that can be easily controlled using a simple PD controller. ADRC consists of two parts, Extended State Observer (ESO) and PD controller. ESO estimates generalized disturbance f and cancels it in real time and PD controller controls the remaining double integral plant. The plant is then written with an extra state:

$$\begin{cases} \dot{y}_1 = y_2 \\ \dot{y}_2 = y_3 + bu \\ \dot{y}_3 = \dot{f} \end{cases} \tag{17}$$

Where $y_1 = x, \quad x_2 = \dot{x}, \quad y_3 = f.$ Based on equation (17) we construct an extended state observer:

$$\begin{aligned} &\dot{z} = Az + Bu + L(x - \hat{x}) \\ &\hat{x} = Cz \end{aligned}$$

$$A = \begin{bmatrix} 0 & 1 & 0 \\ 0 & 0 & 1 \\ 0 & 0 & 0 \end{bmatrix}, \quad B = \begin{bmatrix} 0 \\ b \\ 0 \end{bmatrix}, \quad C = \begin{bmatrix} 1 & 0 & 0 \end{bmatrix} \tag{18}$$

Where $z \to x.$ The observer is reduced to the following state equations:

$$\begin{cases} \dot{z}_1 = z_2 + L_1(x - z_1) \\ \dot{z}_2 = z_3 + L_2(x - z_1) + bu \\ \dot{z}_3 = L_3(x - z_1) \end{cases} \tag{19}$$

The characteristic equation of equations in (19) is $\lambda(s) = |sI - (A - LC)| = s^3 + L_1 s^2 + L_2 s + L_3$, which is equal to the desired error dynamics. The observer gains are set to

$$L_1 = 3\omega_0, \quad L_2 = 3\omega_0^2, \quad L_3 = \omega_0^3 \tag{20}$$

By setting observer gains to equations (20) the system essentially has only one extended state observer tuning parameter ω_0.

As ESO correctly tuned and precisely estimates all of the states including generalized disturbance $z_3 = f$, it is actively cancels the generalized disturbance f by applying the following control signal

$$u = \frac{(u_0 - z_3)}{b} \tag{21}$$

If we combine equations (16) and (21) with an assumption that ESO is precisely tracking f, then the plant reduces to

$$\ddot{x} = (f - z_3) + u_0 \approx u_0 \tag{22}$$

Equation (22) is a representation of a unity gain double integral plant that can be easily controlled using a PD controller

$$u_0 = k_p(r - z_1) + k_d(\dot{r} - z_2) \tag{23}$$

Up to this point the design of ADRC observer was rather general. We assumed that all three states (y_1, y_2, y_3) of the system have to be estimated by the observer in order for system to work. However, this is an assumption for a generalized second order

system, where it is assumed that the outputs of the system (position, velocity) are either unavailable or available but rather noisy. In our particular case, the output signal (x) is readily available and the signal is clean enough that the ESO does not necessarily have to estimate the output of the gyroscope. This particular feature of our system allows us to decrease the order of the observer, which in turn will mean decreased complexity of the design, less hardware required to build an ESO and decrease in cost of the overall system. As mentioned above, it is important to understand that ADRC is an idea that can be applied to a specific problem and does not necessarily follow the same set of equations. This particular case does not require full order ESO to be designed; instead it uses reduced order ESO in which only velocity and generalized disturbance signals are estimated.

Based on (17) the reduced order ESO is constructed:

$$\begin{aligned} &\dot{z} = Az + Bu + L(x - \hat{x}) \\ &\hat{x} = Cz \\ &A = \begin{bmatrix} 0 & 1 \\ 0 & 0 \end{bmatrix}, \quad B = \begin{bmatrix} b \\ 0 \end{bmatrix}, \quad C = \begin{bmatrix} 1 & 0 \end{bmatrix} \end{aligned} \tag{24}$$

From (24) it is clear that the order of the ESO has been reduced. The corresponding state equations are

$$\begin{cases} \dot{z}_1 = z_2 + bu + L_1(x - z_1) \\ \dot{z}_2 = L_2(x - z_1) \end{cases} \tag{25}$$

Where $L_1 = 2\omega_0$, $L_2 = \omega_0^2$ are observer tuning parameters that satisfy characteristic equation $\lambda(s) = \left|sI - (A - LC)\right| = s^2 + L_1 s + L_2$. The control signal of the reduced order ADRC is now

$$u = \frac{u_0 - z_2}{b} \tag{26}$$

By combining equations (16) and (26) the system becomes unity gain double integral plant, which can be easily, controlled using a PD controller

$$u_0 = k_p(r - x) + k_d(\dot{r} - z_1) \tag{27}$$

Notice that the proportional term $k_p(r - x)$ does not contain the estimated output of the system, but uses the measured output fed directly back to the input. Combining equations (26) and (27) the control signal of the system is

$$u = \frac{k_p}{b}(r - x) + \frac{k_d}{b}(\dot{r} - \dot{x}) - \frac{z_2}{b} \tag{28}$$

Where $k_p = \omega_c^{\,2}$, $k_d = 2\omega_c$ with ω_c being the only tuning parameter of the controller. Since the gyroscope operates at rather large resonant frequencies (10-30 kHz), the controller tuning parameter (ω_c) comes out to be a very large value, which would be next to impossible to implement using analog circuit. However, the system's parameter (b) is also a large number and by using equation (28) the large controller gains are scaled down to values that can be implemented in analog hardware without reaching saturation limits.

Although equation (28) can be easily simulated using Matlab, it is a lot harder to implement because of two issues. First, it is impossible to design pure differentiator $(\dot{r} - \dot{x})$ using analog circuit due to stability issues. Second, the estimate of the generalized disturbance (z_2) must be related to generalized disturbance (f) in order to be able to implement generalize disturbance estimation circuit.

Implementation of a differentiator is done by using derivative approximation scheme. Derivative approximate scheme applies differentiation only to a specific operating region or point, where differentiation is required. In this design, the output of the gyroscope x is differentiated only within a specific region in a frequency domain, at resonance. The end of the derivation region is specified by the tuning parameter of the observer ω_0. Representation of the derivative term of equation (28) in Laplace domain is

$$\frac{k_d}{b}(r-x)s \tag{29}$$

After application of derivative approximate scheme the derivative term becomes

$$\frac{k_d}{b}(r-x)\frac{s}{s^2+2\omega_0 s+\omega_0^2} \tag{30}$$

Although first order polynomial could have been used in the denominator of equation (30) ($\frac{s}{s+\omega_0}$) it is always better to add a low-pass filtering action after differentiation in order to eliminate amplified high frequency noise that occurs during differentiation. Combining equation (28) and (30) the updated control signal is

$$u=\frac{k_p}{b}(r-x)+\frac{k_d}{b}(r-x)\frac{s}{s^2+2\omega_0 s+\omega_0^2}-\frac{z_2}{b} \tag{31}$$

The second issue is related to obtaining the relationship between generalized disturbance and estimate of generalized disturbance (f). To show how (z_2) converges to (f) equations (16) and (25) are used. Equation (16) can be rewritten in the following form

$$f=\ddot{x}-bu \tag{32}$$

If $z_2 \equiv f$ was exactly equal to f then the equation (31) would look like this

$$u = \frac{k_p}{b}(r - x) + \frac{k_d}{b}(r - x)\frac{s}{s^2 + 2\omega_0 s + \omega_0^2} - \frac{f}{b} \tag{33}$$

Equation (33) implies that estimation of generalized disturbance in an ideal case ($z_2 \equiv f$) is a unity gain. However in reality there is certain relationship between the two that can be determined by solving equation (25). First, equation (25) and rewritten in the following form

$$\begin{cases} \dot{z}_1 = z_2 + bu + L_1(x - z_1) \\ z_1 = x - \dfrac{\dot{z}_2}{L_2} \end{cases} \tag{34}$$

Combining two equations in (34) the following derivation is yield

$$\dot{x} - \frac{\ddot{z}_2}{L_2} = z_2 + bu + L_1\frac{\dot{z}_2}{L_2} \tag{35}$$

$$L_2(\dot{x} - bu) = \ddot{z}_2 + L_1\dot{z}_2 + L_2 z_2 \tag{36}$$

Converting equation (36) to Laplace domain

$$L_2(sx - bu) = z_2(s^2 + L_1 s + L_2) \tag{37}$$

$$z_2 = (sx - bu)\frac{L_2}{s^2 + L_1 s + L_2} \tag{38}$$

Equation (38) represents the key relationship between generalized disturbance and its estimate. What it states is that estimation of generalized disturbance is simply filtering of the generalized disturbance f. This key concept holds true for any order of (x)

$$z_k = (s^{n-1}x - bu)\frac{L_k}{(s+\omega_0)^k} \tag{39}$$

Therefore, applying equation (39) to estimate f in (32) we obtain

$$\begin{aligned} z_2 &= (s^2 x - bu)\frac{L_2}{s^2 + L_1 s + L_2} \\ z_2 &= f(s)\frac{L_2}{s^2 + L_1 s + L_2} \\ z_2 &= f(s)\frac{\omega_0^2}{(s+\omega_0)^2} \end{aligned} \tag{40}$$

Combining equations (33) and (40) the resulting control signal of the entire ADRC in transfer function form is obtained

$$u = \frac{k_p}{b}(r-x) + \frac{k_d}{b}(r-x)\frac{s}{(s+\omega_0)^2} - x\frac{\frac{\omega_0^2}{b}s^2}{(s+\omega_0)^2} + u\frac{\omega_0^2}{(s+\omega_0)^2} \tag{41}$$

Equation (41) represents ADRC in transfer function form that consists of combination of different types of filters. For better understanding what types of filters are used in this design, equation (43) can be rewritten in the following form

$$u = P\cdot(r-x) + BPF\cdot(r-x) - HPF\cdot(x) + LPF\cdot(u) \tag{42}$$

Where

$$
\begin{aligned}
Proportional\ Gain(P) &= \frac{k_p}{b} \\
Band\ Pass\ Filter(BPF) &= \frac{\frac{k_d}{b}s}{(s+\omega_0)^2} \\
High\ Pass\ Filter(HPF) &= \frac{\frac{\omega_0^2}{b}s^2}{(s+\omega_0)^2} \\
Low\ Pass\ Filter(LPF) &= \frac{\omega_0^2}{(s+\omega_0)^2}
\end{aligned}
\tag{43}
$$

Filters in equation (43) are all implemented using pure active analog circuits (operational amplifiers, resistors, capacitors). The resonant frequency of the gyroscope is quite high, therefore it is important to spec out operational amplifiers to have high operational bandwidth and high slew rate in order to avoid signal lags and phase distortion.

Although the design process seems to be complex, the resulting controller is quite simple. It only consists of an amplifier (proportional gain) and three second order filters, which are all easily realizable in an analog circuit. Yet, the simplicity combined with high performance are the key elements that separate analog ADRC from many other types of advanced controllers. The power of analog ADRC is that the controller design becomes intuitive in nature, because the entire design is based on intelligent combination of different types of filters. Ones the designer understands the purpose of each filter, tedious mathematical derivation can be omitted and simple, low-cost and high performance controller can be implemented relatively quickly.

2.2 Analog ADRC Circuit Design

The entire design of analog ADRC circuit is done using pure analog components such as operational amplifiers, resistors and capacitors. Equation (42) contains all of the control loop parameters including low-pass, high-pass and band-pass filters, amplifier for proportional gain, summation and subtraction junctions. It is important to note that each individual component in equation (42) must be designed separately to insure the correctness of operation. Once all of the components are designed and operation is verified, they can be integrated together to complete the overall control loop.

The first component of equation (42) to be designed is a two-input subtraction junction

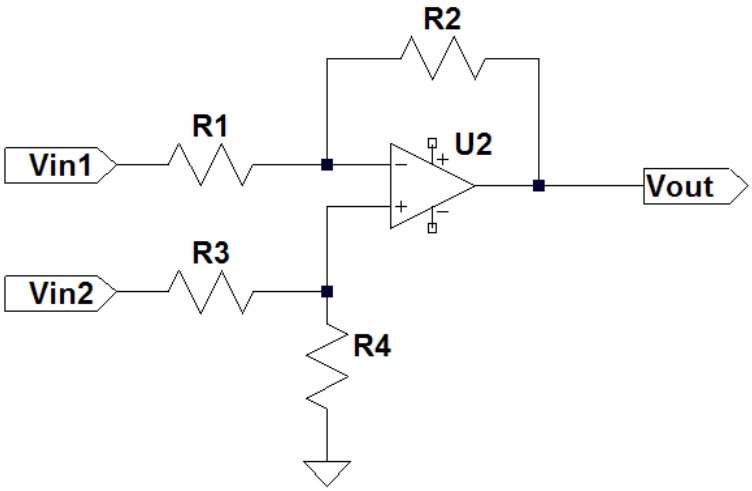

Figure 6: Two-Input Subtraction Junction

Subtraction circuit takes two inputs, Vin1 and Vin2 and outputs the difference between them

$$V_{out} = \frac{R_4}{R_3} V_{in2} - \frac{R_2}{R_1} V_{in1} \tag{44}$$

The ration of resistors for each voltage input determines the gain of each signal. Since this design does not require any particular amplification, all resistors are equal $R_1 = R_2 = R_3 = R_4$ and equation (44) becomes

$$V_{out} = V_{in2} - V_{in1} \tag{45}$$

Another arithmetic circuit is an addition circuit that is shown in figure 7

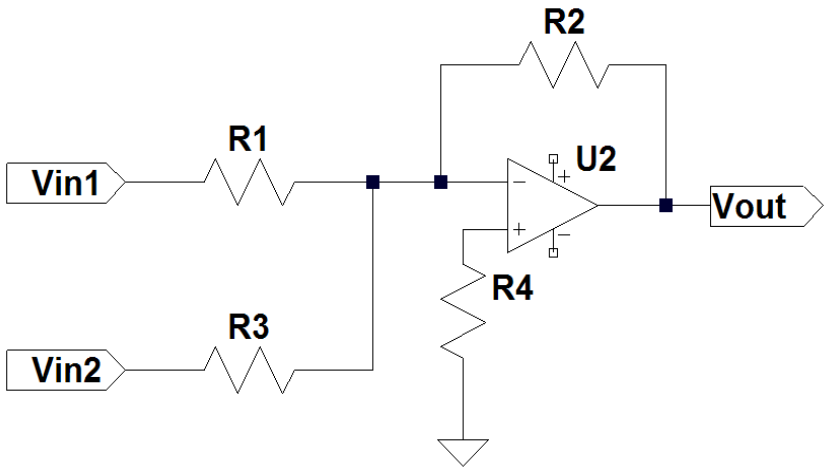

Figure 7: Addition Circuit

Addition circuit takes two inputs, Vin1 and Vin2, and adds them together to represent Vout

$$V_{out} = -(\frac{R_2}{R_1} V_{in1} + \frac{R_2}{R_3} V_{in2}) \tag{46}$$

By making all resistors equal the output is

$$V_{out} = -(V_{in1} + V_{in2}) \tag{47}$$

Although both input voltages are added, the output voltage is inverted. If the inversion is not desired, additional inverting buffer can be added to the output. In our design it is not required because the inverted output is an intermediate signal and is accounted for in the later stages of the design.

Another part of the controller design is a proportional gain, which is simply an amplifier circuit

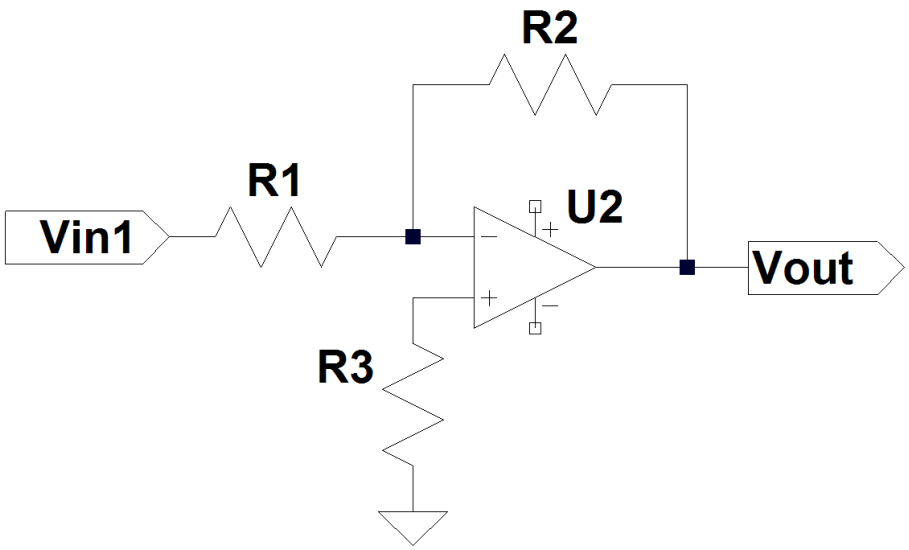

Figure 8: Amplifier Circuit

Amplifier circuit takes input voltage Vin1 and outputs the amplified voltage Vout

$$V_{out} = -\frac{R_2}{R_1} V_{in1} \tag{48}$$

The ratio of resistors R_1 and R_2 determines the amount of amplification

$$Proportional\ Gain = \frac{R_2}{R_1} \tag{49}$$

Since inverting amplifier is used, the output voltage is inverted. One way to avoid it is to use non-inverting amplifier, in which case the proportional gain will become

$$Proportional\ Gain = 1 + \frac{R_2}{R_1} \tag{50}$$

Yet, it is not required for this design, since the inverted amplified signal can be accommodated in later stages of the design.

Up to this point, all of the shown circuits only dealt with amplitude of input and output signals. Next three circuits (LPF, HPF, and BPF) affect both the amplitude and frequency of inputs and outputs. The first circuit to be designed is a non-resonant second order low-pass filter (LPF). There are many different types of low-pass filter topologies and their complexities and tuning options depend on the application they are used for. In this application, one tuning parameter low-pass filter would be the best solution to achieve desired simplicity. The equal component value Sellen Key low-pass filter is a perfect fit for the requirements of the design

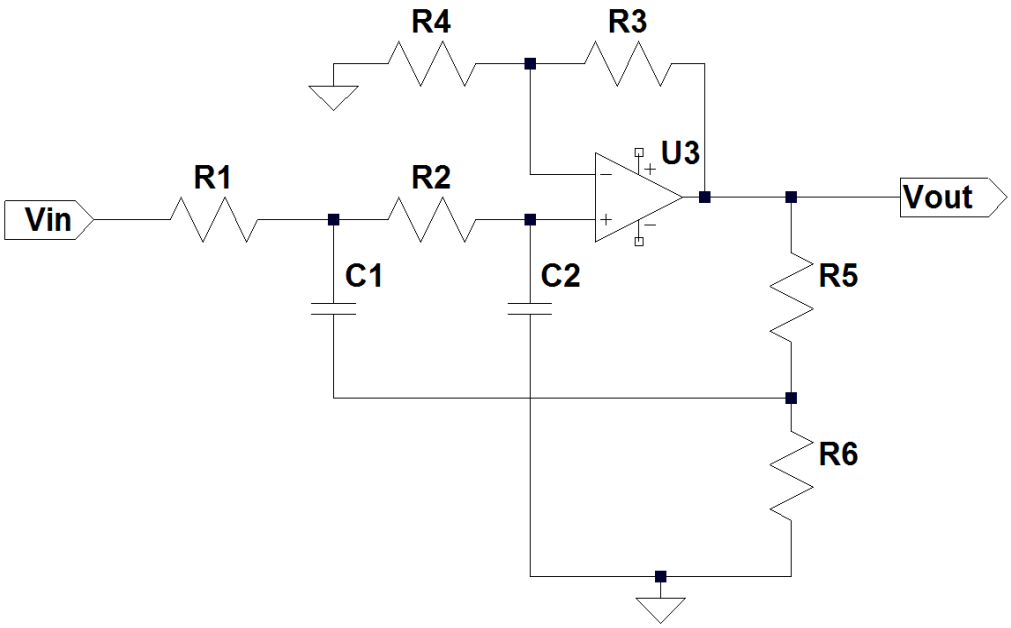

Figure 9: Sallen Key Low-Pass Filter

The circuit in Figure 9 represents low-pass Butterworth response with resistors $R_1 = R_2$ and capacitors $C_1 = C_2$ (equal component circuit). The cutoff frequency of the filter is

$$\omega_{cutoff} = \frac{1}{\sqrt{R_1 R_2 C_1 C_2}} \tag{51}$$

Since the resistors and capacitors are equal in values the equation (51) can be further minimized

$$\omega_{cutoff} = \frac{1}{R_1 C_1} \tag{52}$$

This means that the filter has only one tuning parameter and can be adjusted by changing the value of either resistor R_1 or capacitor C_1. The addition of resistors R_5 and

R_6 creates the resistive gain enhancement, which means that the filter has variable gain for fine tuning of a signal.

The same approach was taken is designing a high-pass filter. The equal component value Sallen Key high-pass filter is chosen

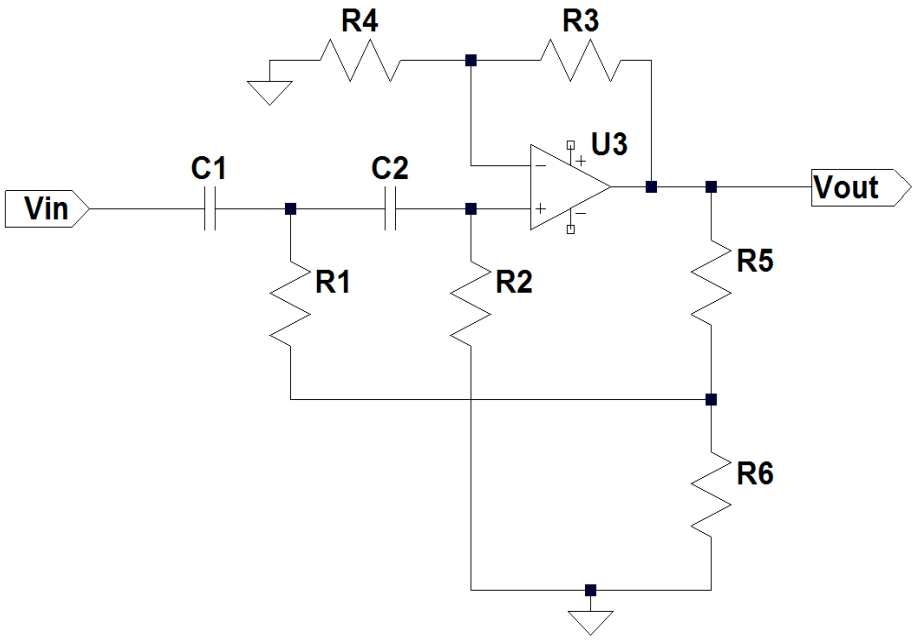

Figure 10: Sallen Key High-Pass Filter

The filter in Figure 10 is a non-resonant high-pass Butterworth filter. It apparent that the only difference between Sallen Key low-pass filter and Sallen Key high-pass filter is the position of tuning resistors and capacitors. The cutoff frequency of the high-pass filter is the same as the low-pass one

$$\omega_{cutoff} = \frac{1}{R_1 C_1} \tag{53}$$

High-pass filter also has the resistive gain enhancement circuitry in order to fine tune the output. Both filters have similar structure with only one tuning parameter. This

choice for filter design provides simplicity, but yet very powerful high-performance system.

Any filter designer will find that there are many types of band-pass filters circuits available to realize the second order band-pass response. From the large number of possibilities, most designers will chose the design that they are either very comfortable with or it's the simplest for the particular application. For this design the choice has to go with the simplest and easy to tune one. We choose a very famous and useful Delyiannis-Friend band-pass filter

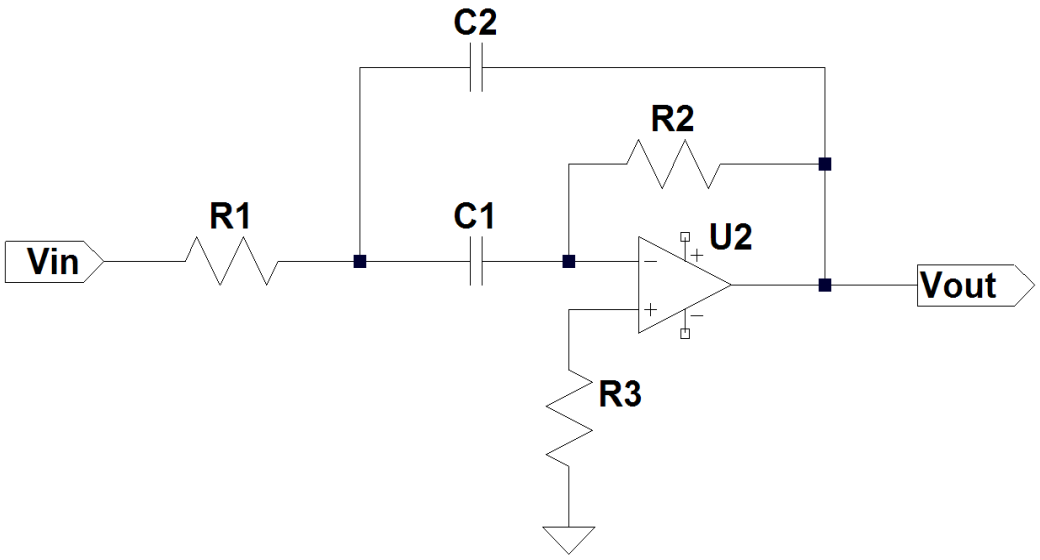

Figure 11: Delyiannis-Friend Band-Pass Filter

Just like with the low-pass and high-pass filter, the Delyiannis-friend band-pass filter has one tuning parameter and the cutoff frequency is

$$\omega_{cutoff} = \frac{1}{C\sqrt{R_1 R_2}} \tag{54}$$

Where $C = C_1 = C_2$ and resistors R_1 and R_2 determine the gain of the filter for fine tuning. During implementation, the capacitors can be physically connected together on the same shaft (change value at the same time) and one of the resistors can be used to tune quality factor (Q) or bandwidth of the filter (BW).

All three filters have very simple design approach with each having one tuning parameter and ability to be fine tuned. During implementation, all of the tuning components can be physically connected on the same shaft, creating one physical tuning parameter (knob) for all three filters.

The following chapter will show how the above circuits interact with one another to produce high-performance controller. The simulation results of analog ADRC by using Matlab/Simulink for block diagram representation and LTSpice for circuit simulation is shown next.

CHAPTER III

SIMULATION RESULTS

The simulation part of the sensor development is divided into two parts. First, the simulation of ADRC controller on VBG is done using Matlab/Simulink in order to verify the operation of the controller on both drive and sense axis. Second part is the verification of the controller operation using LTSpice circuit simulator. Although both simulations verify the correctness of controller operation, what they help to determine is quite different. Simulations using Matlab helps to correctly tune controllers (determine the values for tuning parameters) for both axis and verify the controller's tracking precision. The results obtained using Matlab simulations are empirical and do not contain information on how to build hardware to produce such results. In order to translate empirical results into actual hardware, we use LTSpice circuit simulator. It takes tuning parameters values (ω_0 , ω_c), which represent observer and controller frequencies, and use them to determine the actual values of circuit components (resistors, capacitors). Once the simulation results produced by Matlab are matched with simulation results produced

by LTSpice, the actual hardware can be build to produce experimental results, which will be compared to simulation ones.

3.1 Analog ADRC Matlab Simulation

The simulation of MEMS gyroscope is done using a Vibrating Beam Gyroscope model from University of Alabama. The mathematical representation of the model is given in equations (3) and (4) with key parameters being $\omega_x = 63428.25\ rad/s$, $\omega_y = 63365.20\ rad/s$, $\xi_x = 5\times10^{-4}$, $\xi_y = 4.89\times10^{-4}$, $m = 4\times10^{8}$, $\omega_{xy} = 6000\ rad^2/\sec^2$.

Using equation (41) the block diagram of ADRC for drive and sense axis is constructed. Figure 12 and Figure 13 show the block diagram of drive and sense axis, respectively

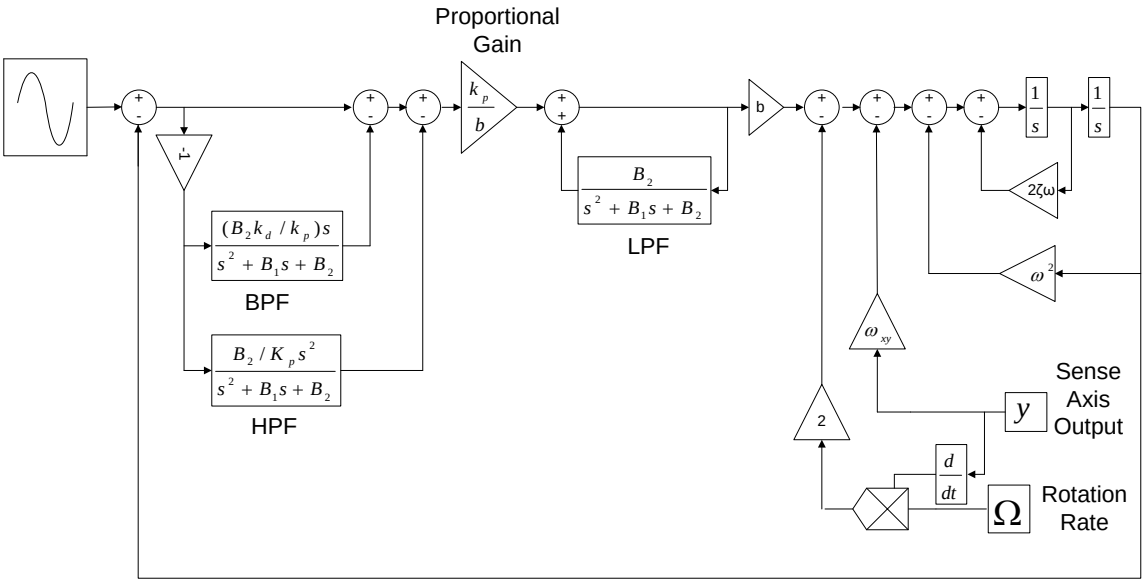

Figure 12: Block Diagram of Drive Axis

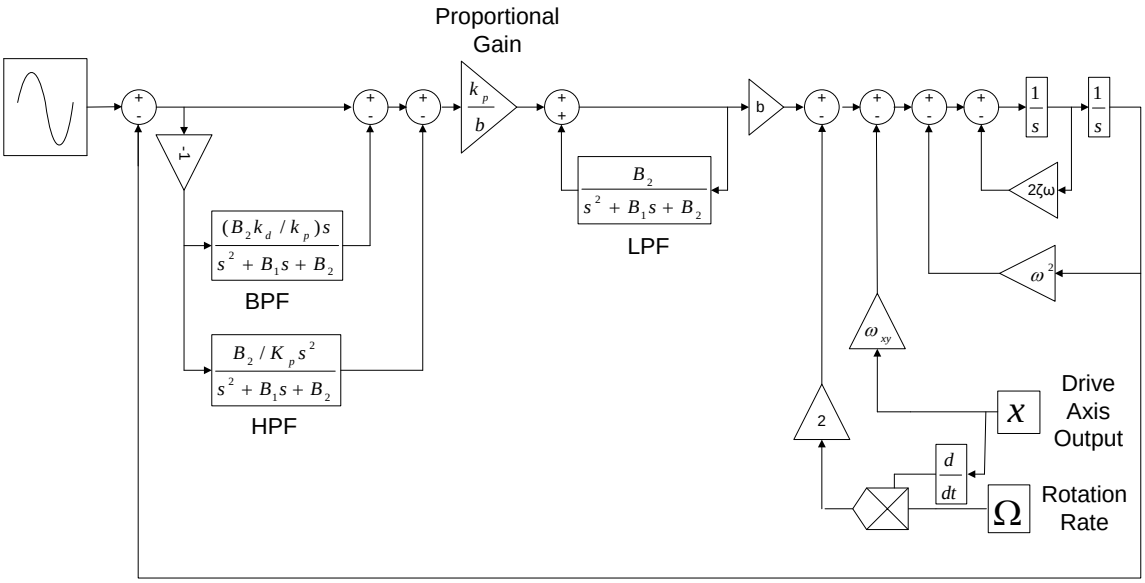

Figure 13: Block Diagram of Sense Axis

Both block diagrams demonstrate the coupling relationship between drive and sense axis by having an extra input to each plant, $\omega_{xy}x$ and $\omega_{xy}y$ respectively. In addition, Coriolis acceleration signals are added to both block diagrams to fully represent

gyroscope model from equations (3) and (4). The only difference between the block diagrams is the reference signal. The reference signal for drive axis is a sinusoidal function

$$r_{drive} = A\sin(\omega_x t) \tag{55}$$

The amplitude A is set to 100 in "Matlab units", which during implementation would correspond to $\pm 100mV$. The reason the amplitude A is relatively small is because the physical device has an input limitation of $\pm 200mV$, therefore exciding this voltage might permanently damage the device. Since the control goal is to force and maintain drive axis at resonance, the reference signal frequency ω_x is set to the resonant frequency of drive axis.

Unlike the drive axis, the reference signal of sense axis is set to zero

$$r_{sense} = 0 \tag{56}$$

The force-to-rebalance control methodology that is employed for sense axis forces and maintains the output signal at zero.

In order for controller to perform at its highest capacity, it must be tuned well. ADRC has two main tuning parameters, observer and controller tuning parameters, ω_0 and ω_c, respectively. From Figure 12 and 13, both parameters are affecting the response of the filters, but each in its own unique way. Observer parameter ω_0 can be understood as a bandwidth of the observer or the cutoff frequency of observer filters. Theoretically, the higher the bandwidth of the observer, the higher performance can be obtained, however, it is not the case in reality. Any system has a point after which the

increase of the observer bandwidth does not improve the performance of the system, instead it gets worse. When observer bandwidth is set too high, more high frequency noise is allowed in the system, which degrades its performance. The conclusion from this observation is that any system has a range within which, the observer tuning parameter can be set to provide the best performance. Generally, the range is pretty wide and can very well include high frequency noise region. In that case, there is a trade off between high bandwidth (higher performance) and amount of high frequency noise allowed. The decision on how high the observer bandwidth should be set is solely depending on the application and designers choice.

On the other hand, the controller bandwidth ω_c determines the response time of the observer as well as the PD controller. Theoretically, the higher the value of ω_c, the faster the response time of the overall system. However, just like in the case with observer bandwidth, controller bandwidth has its own limitations. From Figure 12 and 13, the controller bandwidth determines the proportional gain value, and, therefore, has a finite range within which it can be set. If ω_c is set too high, then the system's response will contain overshoot and may even lead to oscillations and instability.

There are many ways ADRC controller can be tuned and it is hard to choose one that is the best, since the applications are all very different. However the presence of boundaries for both tuning parameters makes it easier to define the range of operation and fine tune the controller to achieve the best performance. One definite rule in any system, and in this design in particular, is that both tuning parameters must be higher then the plants operating bandwidth. Taking into account above information, the following procedure demonstrates how the ADRC was tuned to control vibrating beam gyroscope.

Knowing that the resonant frequency of VBG is around 10 kHz, the controller tuning parameter was first set to the highest value before overshoot occurred. At the same time, the observer tuning parameter was randomly set to a value that is about ten times higher then the resonant frequency of the gyroscope. Running simulations with this set of parameters yielded poor tracking performance, which meant that the observer parameter was set too low. After increasing the observer parameter number of times, the performance of the controller improved, until the observer upper boundary was met ($\omega_c = 4\times10^5\ rad/s$). Any increase of ω_c beyond this value yielded no improvement in tracking. Important thing to note is that the controller tuning parameter should not be changed during observer tuning and vice versa. After the fine tuning of the observer parameter, the final values were set to be

$$\begin{aligned}\omega_c &= 2\times10^5\ rad/s\\ \omega_0 &= 4\times10^5\ rad/s\end{aligned} \tag{57}$$

The above tuning procedure is unique for this particular application and can be used as a general guideline for tuning ADRC controller. However, the values in equation (57) will not necessarily work for another application.

The following simulation results are obtained using parameter values of equation (57). The first simulation result is the response of the drive axis to a sinusoidal input

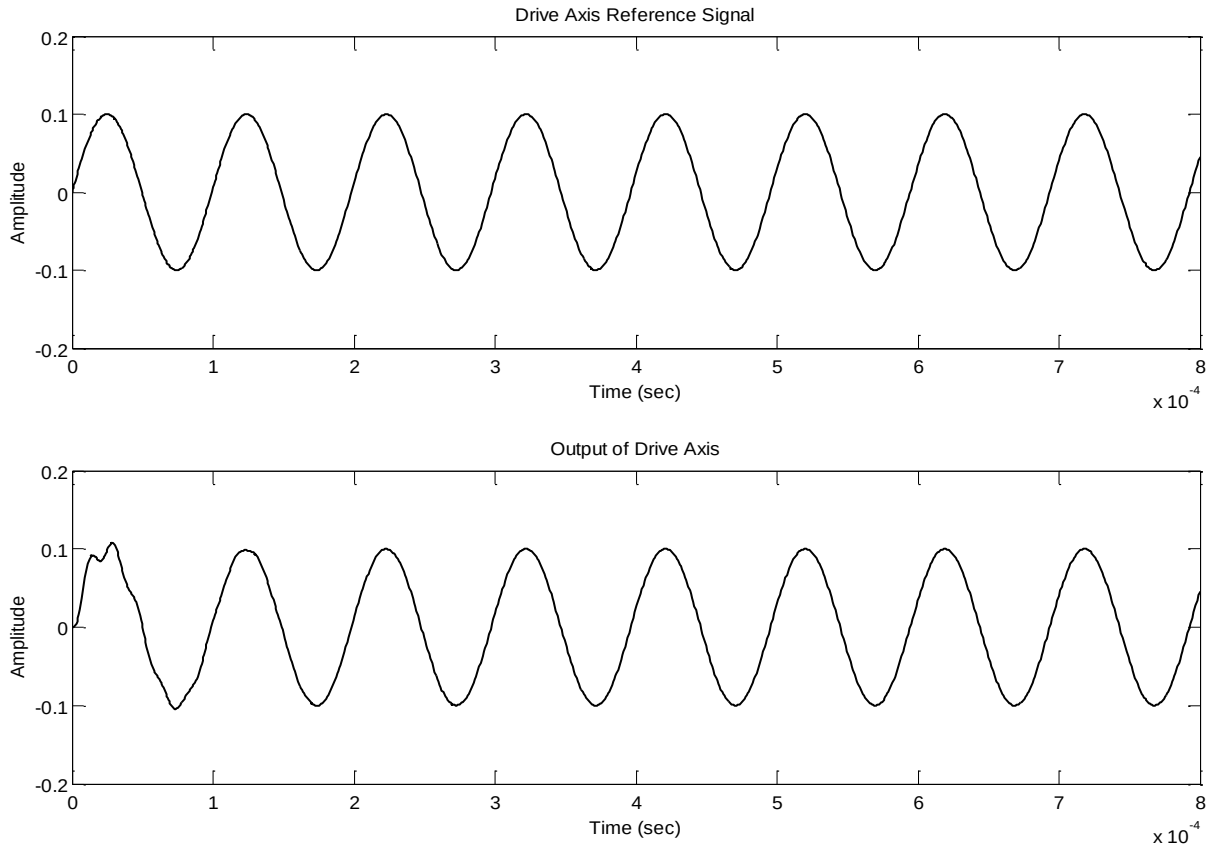

Figure 14: Input and Output of Drive Axis

From Figure (14), the output of the drive axis (bottom) is perfectly tracking the reference sinusoidal input. The transient of the output contains a small overshoot that is within the specified margins, and is very fast, approximately $60\mu s$. The amplitude and frequency are constant and stable during the operation.

The control signal of the drive axis is

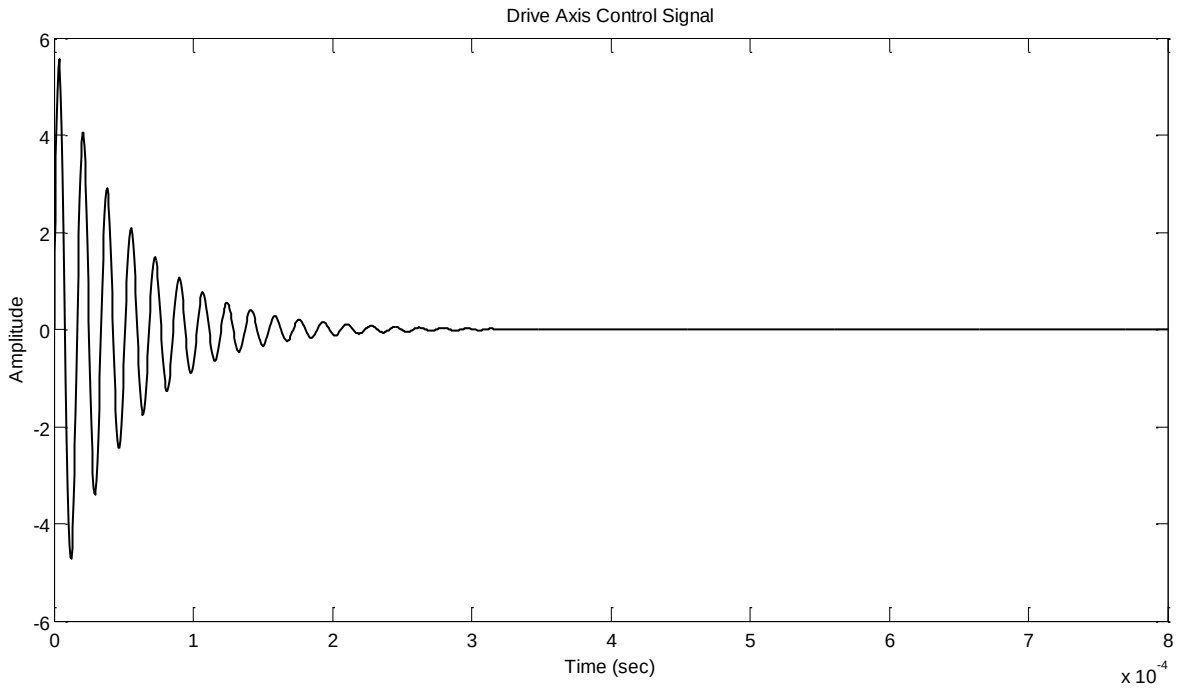

Figure 15: Control Signal of Drive Axis

In the initial moment of operation, the system requires a large control signal to achieve the desired set point, which is evident from Figure 15. Once the set point is reached, the control effort is starting to exponentially decrease. Note how the transient time of the control signal matches the transient time of the output of drive axis.

So far, the discussion was about the position output of the drive axis. However the ESO also has estimated velocity and acceleration signal. In order to show how he estimated velocity converges to the measured one, Figure 16 represents the difference between them ($\dot{x} - z_1$)

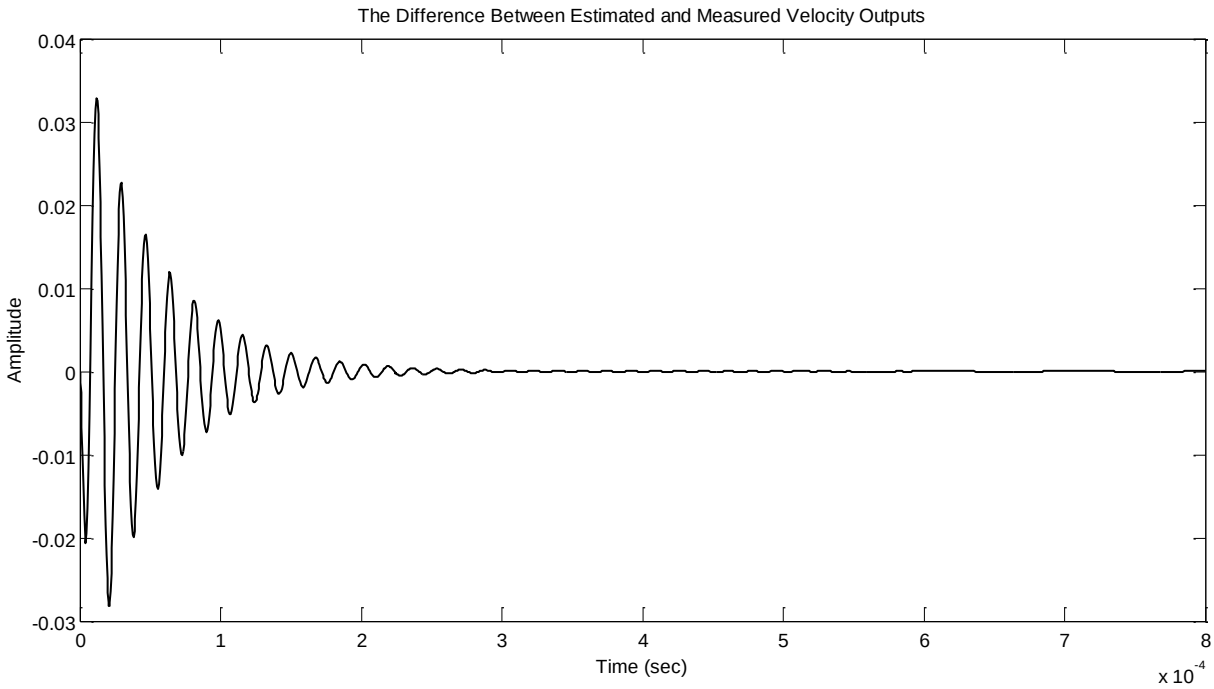

Figure 16: The Estimated vs Measured Velocity Outputs

During transient period there is a difference between estimated velocity and the measured one. However, in the steady state the difference is very small and can be considered to be zero for all practical purposes. The same holds true for the difference between estimated acceleration and measured one

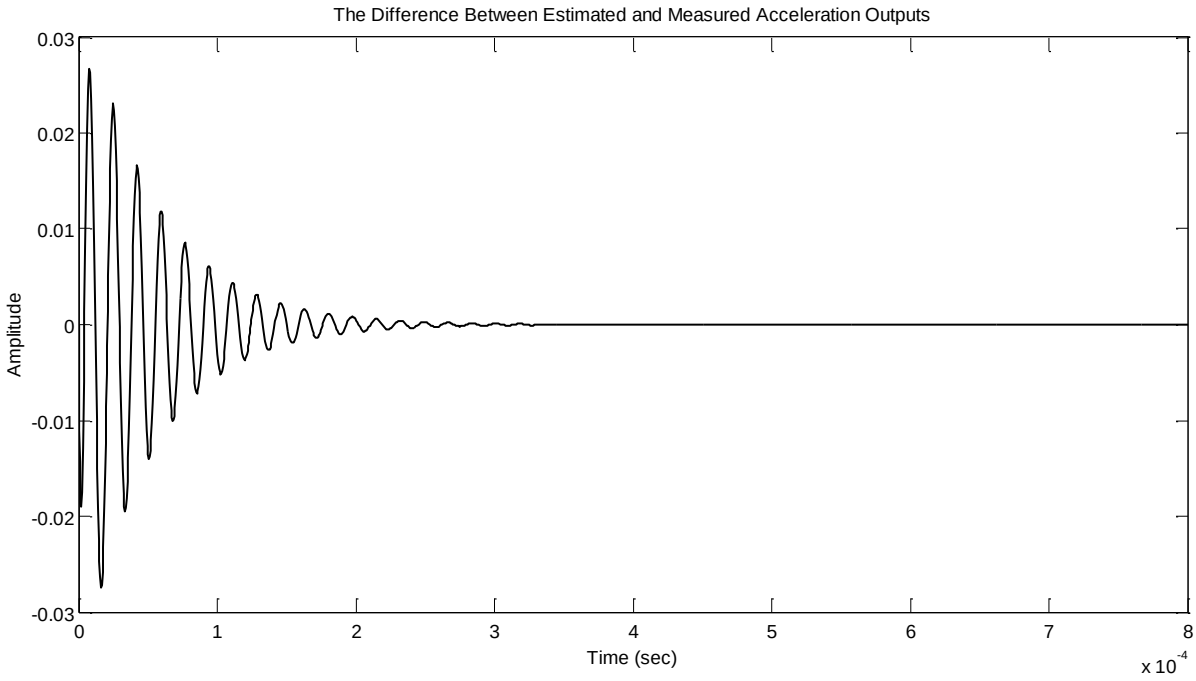

Figure 17: Estimated vs Measured Acceleration Outputs

The next of results describes the results obtain by running simulations with sense axis control. Figure 18 shows the response of the sense axis output to the applied zero reference signal

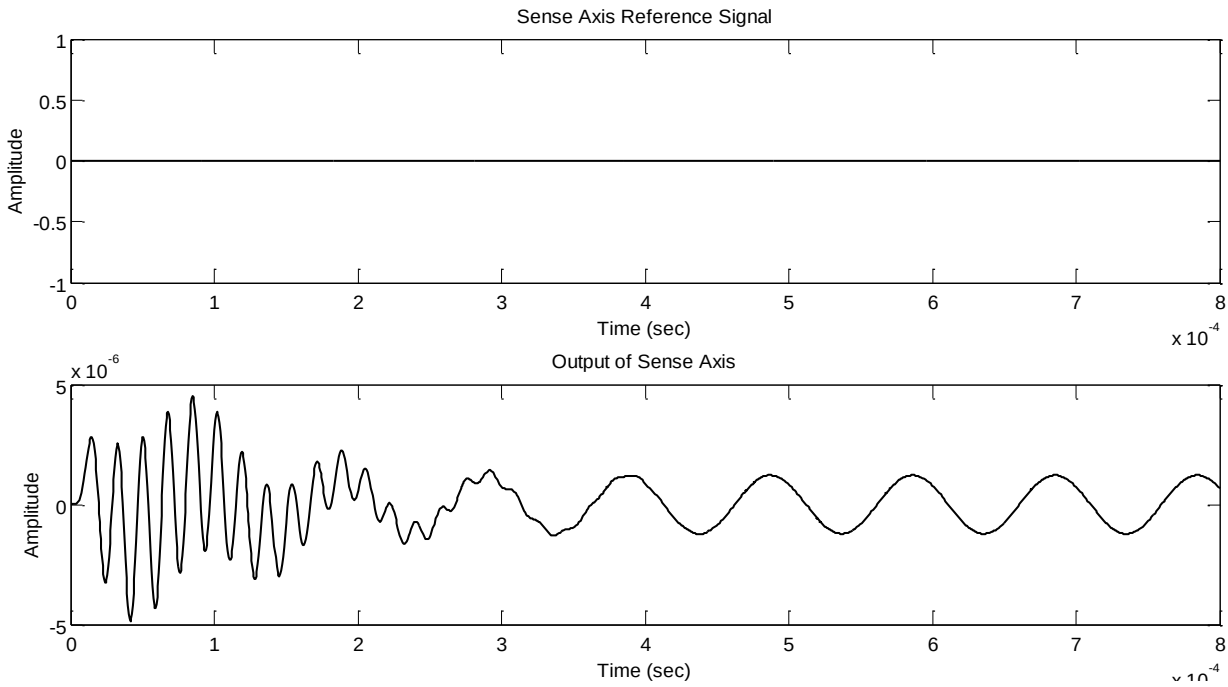

Figure 18: Input and Output of Sense Axis

The Figure 18 shows small amplitude sinusoidal instead of expected zero output. However, the amplitude of the output is in the magnitude of micro-volts, which is well within the noise floor of an analog signal. Therefore, for all practical purposes the output of sense axis can be considered to be zero.

Unlike control signal of drive axis, the control signal of sense axis contains the rotation rate information and is expected to be a sinusoidal in milli-volts range

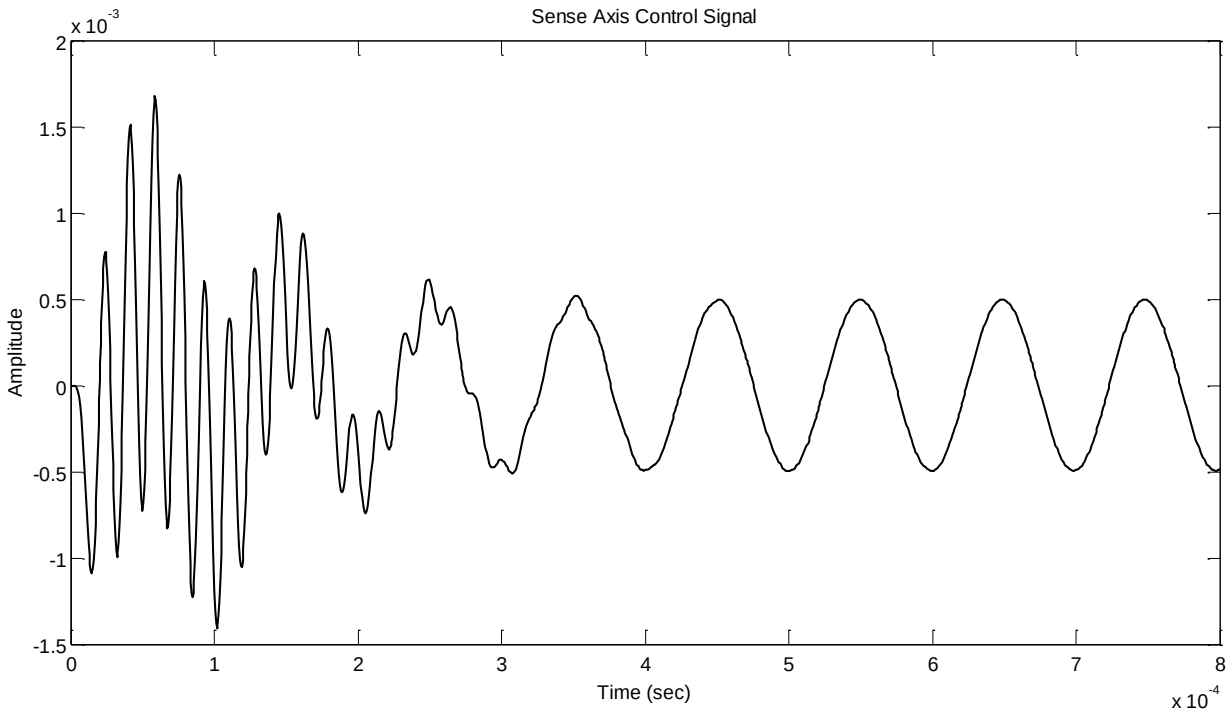

Figure 19: Control Signal of Sense Axis

Figure 19 shows how after a certain period of transient, the output reaches a steady state, which is represented by a constant amplitude and frequency sinusoidal. The steady state is reached within 200 micro seconds and contains the rotation rate information

$$u_{drive} = w_{xy}x + 2\Omega\dot{x} \tag{58}$$

By demodulating this signal and applying signal conditioning, the rotation rate can be extracted and displayed.

The velocity and acceleration outputs of sense axis are also estimated to ensure their convergence. The following figures show the difference between the estimated and the measured velocity and acceleration signals

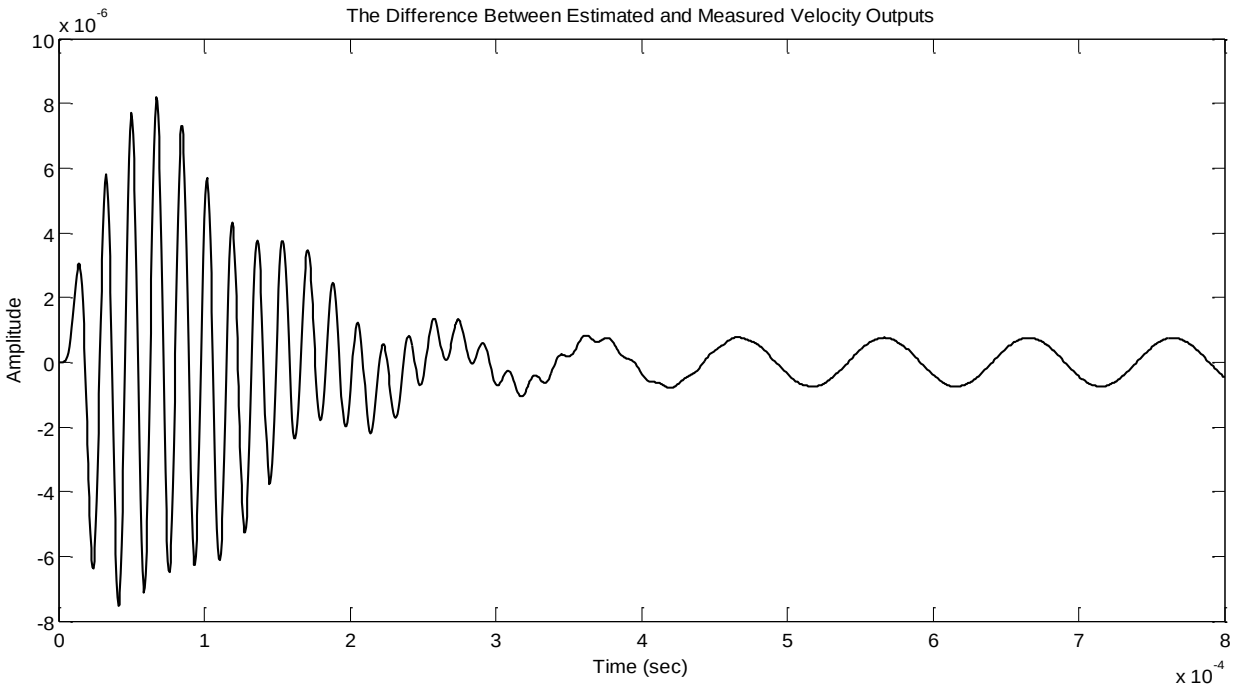

Figure 20: Estimated vs Measure Velocity Output

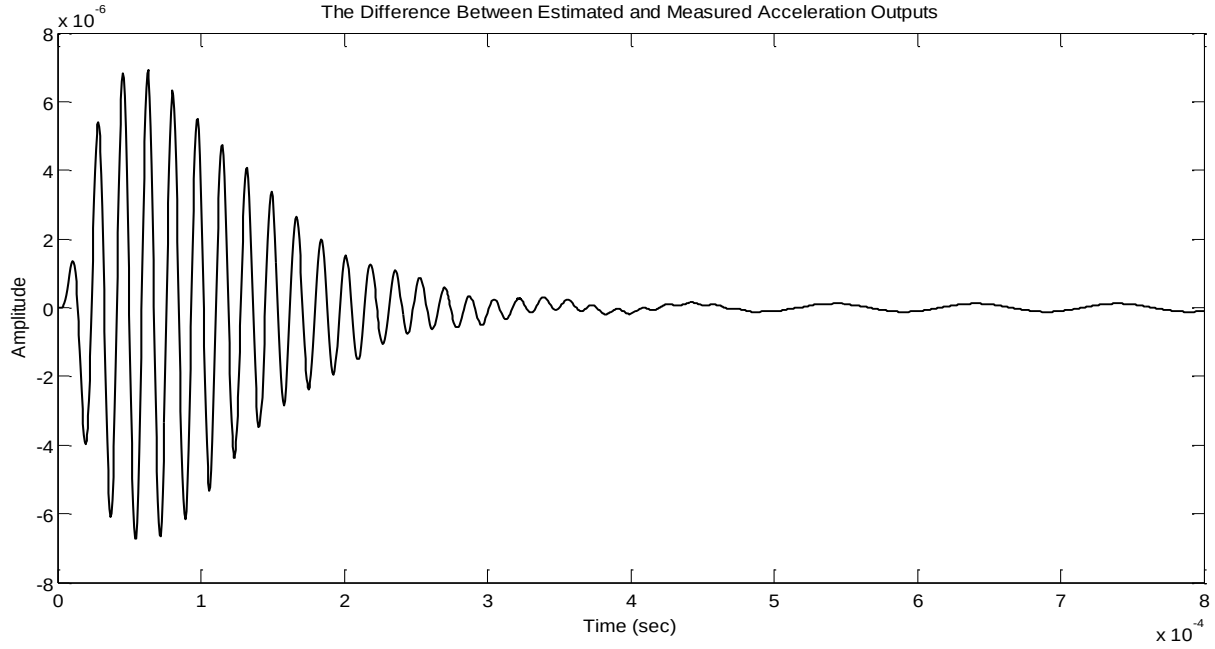

Figure 21: Estimated vs Measured Acceleration Output

Figure 20 and 21 show the convergence of the difference between estimated velocity and acceleration and the measured signals.

3.2 Analog ADRC Circuit Simulation

The above simulation results demonstrate the controller operation and performance. However, these results are empirical and do not show how to develop hardware to obtain the same results during implementation. In order to achieve the same results in hardware, the controller of Figure 12 and 13 must be converted to actual circuit and simulated using LTSpice circuit simulator. The main building blocks of ADRC are the low-pass, high-pass and band-pass filters; therefore, the main focus is on designing filters that meet the specifications of equation (57). All three filters are designed using pure analog circuits and operation is verified in time and frequency domains.

The first filter to be designed is an equal component Sallen Key non-resonant low-pass filter of Figure 9

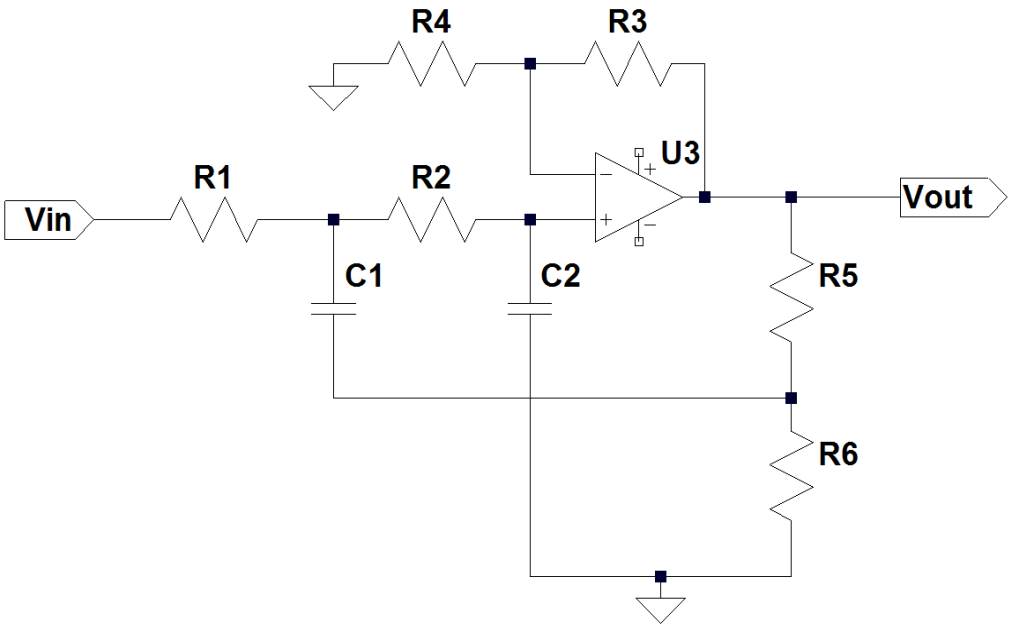

Figure 22: Sallen Key Low-Pass Filter

The mathematical representation of the low-pass filter is given in equation (43). Its cutoff frequency is given in equation (57) and by using equation (52) the values for resistors (R_1, R_2) and capacitors (C_1, C_2) can be calculated. The resistors value is taken to be $R_1 = R_2 = 10k\Omega$ and after calculating the capacitors value it come out to be $C_1 = C_2 = 250\,pF$. The rest of the resistors (R_3, R_4, R_5, R_6) are given values so the overall gain of the filter is unity, that is $R_3 = 0$, $R_4 = 39k\Omega$, $R_5 = 0$, $R_6 = 39k\Omega$.

To verify that the above values are chosen correctly and filter operates properly, its frequency response, obtained from a circuit simulation, is compared to the frequency response of the low-pass filter from equation (43) simulated in Matlab

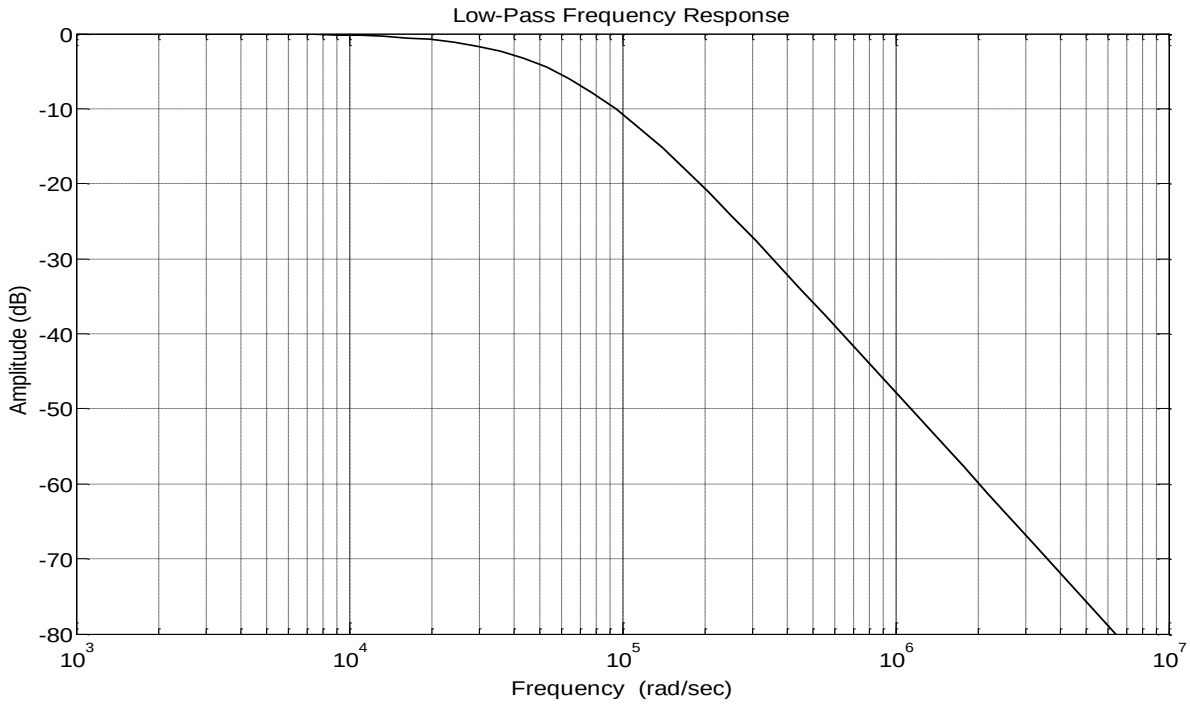

Figure 23: Low-Pass Filter Frequency Response using Matlab

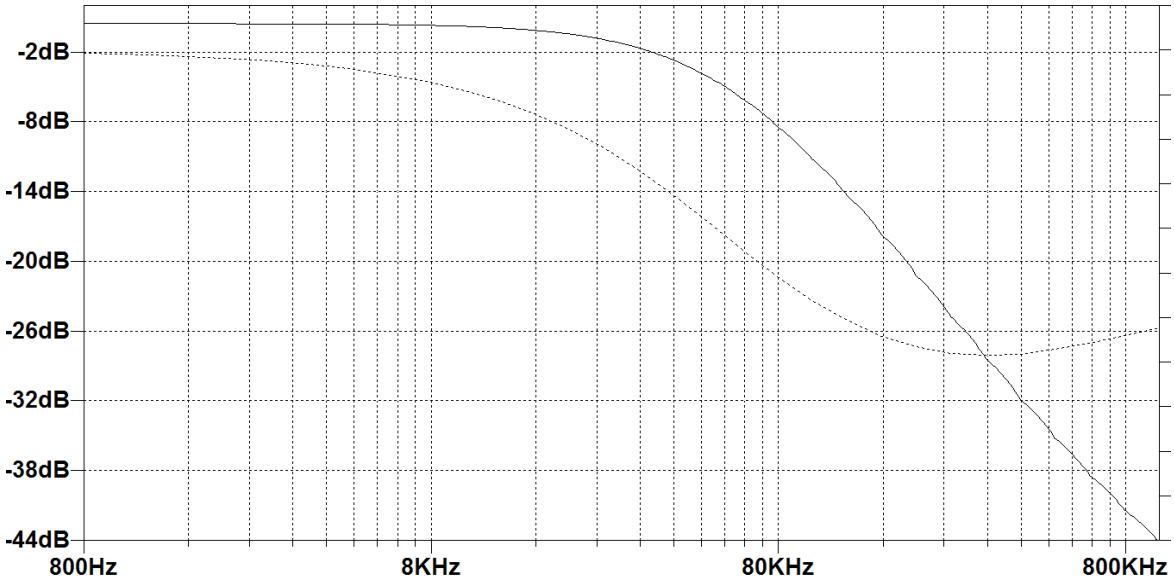

Figure 24: Low-Pass Filter Frequency Response using LTSpice

From Figures 23 and 24 it is apparent that the filter responses are almost identical. Cutoff frequency of both figures is $\omega_0 = 4 \times 10^5 \, rad/s$, which is indicated by a $-6dB$ amplitude level. The pass band region is at $0dB$ level, which indicates unity gain, and it includes the resonant frequency of the VBG ($\omega_x = 63.428 \times 10^3 \, rad/s$), which is approximately six times lower than the attenuation region of the filter. To show flat pass band capability, the LPF circuit is simulated with a sinusoidal signal. The frequency of the sinusoid is set to $10.1kHz$ and amplitude to $100mV$. After running the simulation the following is the output of the LPF

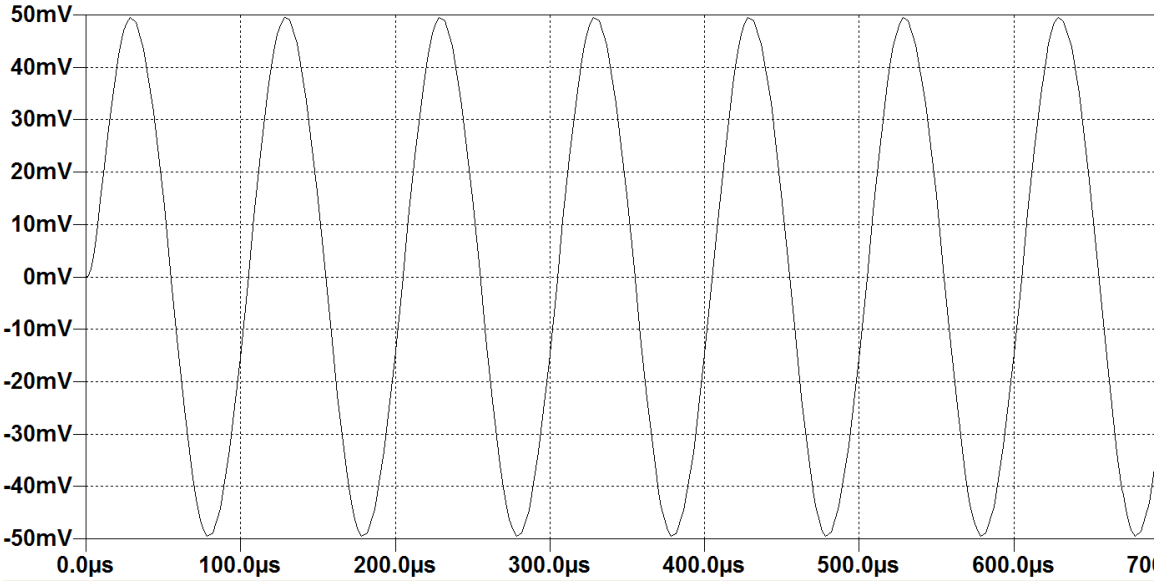

Figure 25: The LPF Time Response

Although the circuit design precisely matched the Matlab simulation results, during implementation the signal levels are not going to be ideal. Taking this into account, the values of the LPF filter components are not constant and are subject to possible change.

The second filter to be designed is a equal component Sallen Key non-resonant high-pass filter of Figure 10

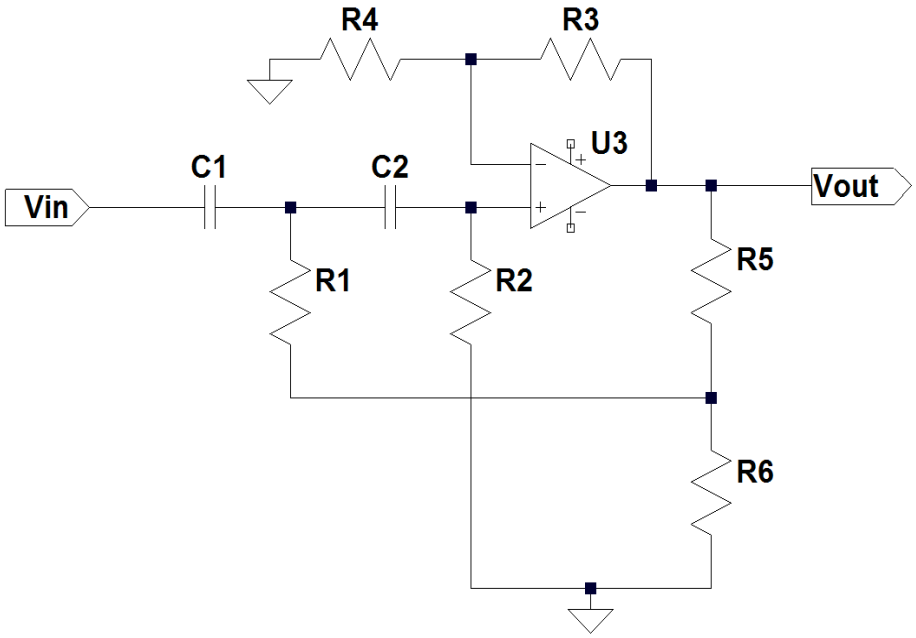

Figure 26: Sallen Key High-Pass Filter

The mathematical representation of the high-pass filter is given in equation (43). Its cutoff frequency is given in equation (57) and by using equation (52) the values for resistors (R_1 , R_2) and capacitors (C_1 , C_2) can be calculated. The resistors value is taken to be $R_1 = R_2 = 10k\Omega$ and after calculating the capacitors value it come out to be $C_1 = C_2 = 250\ pF$. The rest of the resistors (R_3 , R_4 , R_5 , R_6) are given values so the overall gain of the filter equals to four, that is $R_3 = 29k\Omega$, $R_4 = 10k\Omega$, $R_5 = 10k\Omega$, $R_6 = 10k\Omega$.

To verify that the above values are chosen correctly and filter operates properly, its frequency response, obtained from a circuit simulation, is compared to the frequency response of the low-pass filter from equation (43) simulated in Matlab

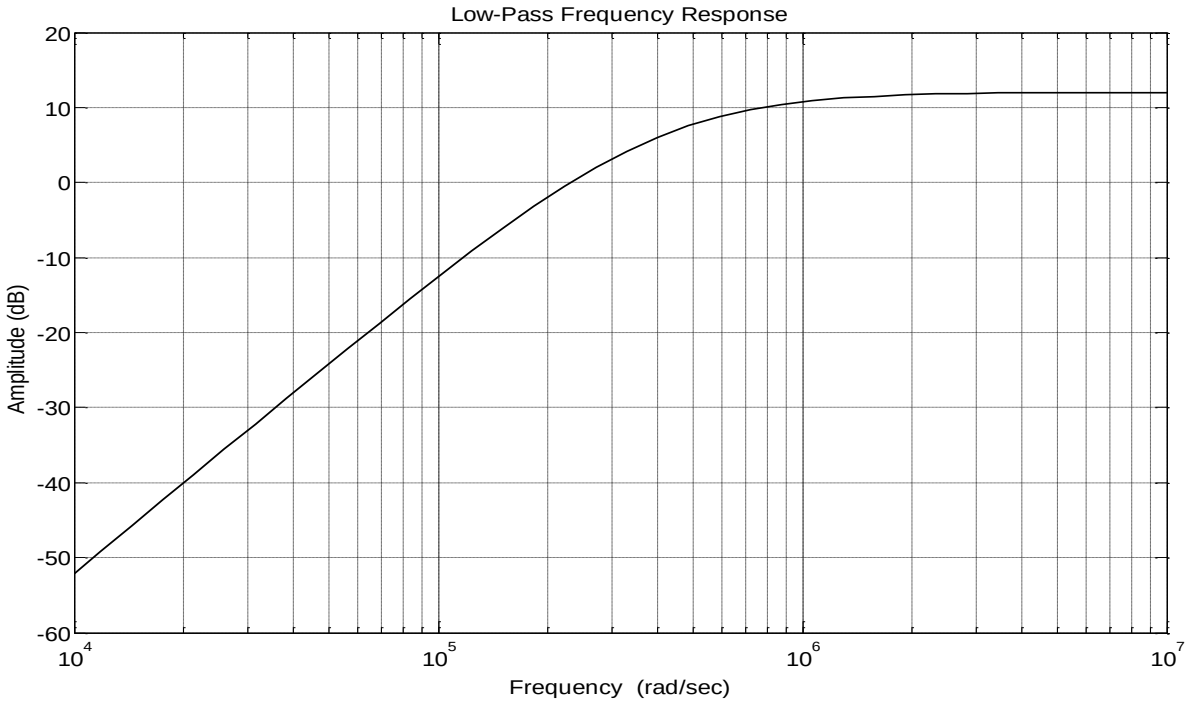

Figure 27: Frequency Response of High-Pass Filter using Matlab

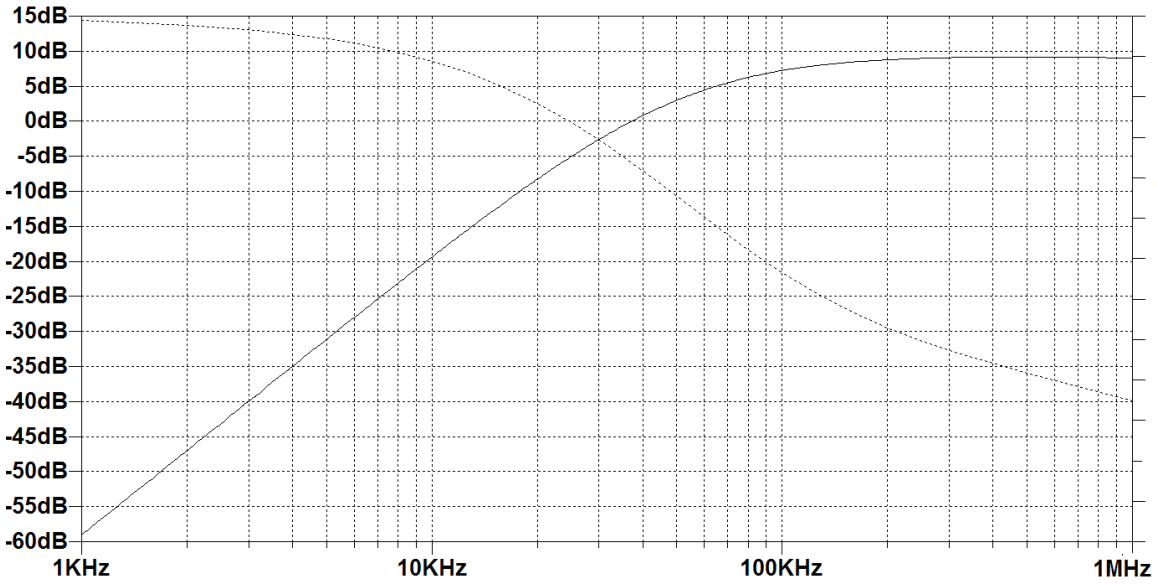

Figure 28: Frequency Response of a High-Pass Filter using LTSpice

High-pas filter response of Figure 28 is identical of the one in Figure 27. The region of differentiation ends at cutoff frequency $\omega_0 = 4 \times 10^5 \, rad/s$ and includes the operation frequency of the gyroscope ($\omega_x = 63.4 \times 10^3 \, rad/s$). Important thing to note is that the region of differentiation is located below $0dB$, therefore, the differentiated signals are small in amplitude. Adding to poles to the differentiator (derivative approximation) essentially ensures that the system is bounded within certain limits and will not go unstable.

In order to demonstrate the operation of a high-pass filter in time domain, the circuit is simulated with the same sinusoidal as it was with a low-pass filter

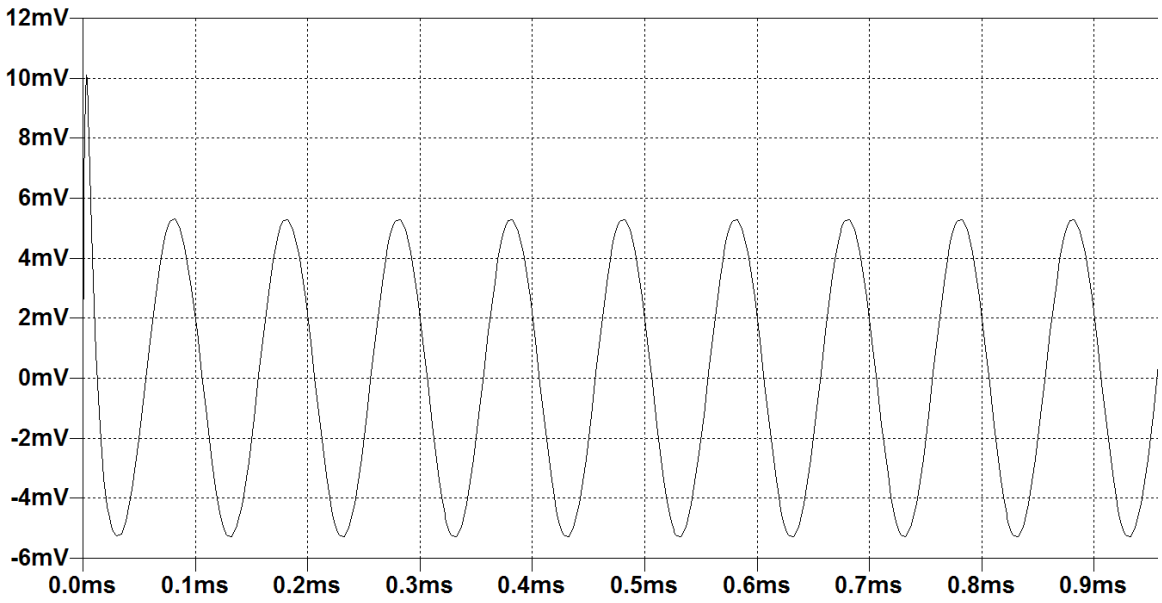

Figure 29: Operation of a High-Pass Filter in Time Domain

Figure 29 show that high-pass filter essentially attenuates the signals. The input sinusoidal has amplitude of 50mV and the output is approximately 5mV. The attenuation occurs because the frequency of input sinusoidal is at 10 kHz and this point in frequency domain (Figure 28) corresponds to approximately -20dB of attenuation.

The third and last filter to be designed is a Delyiannis-Friend Band-Pass Filter of Figure 11

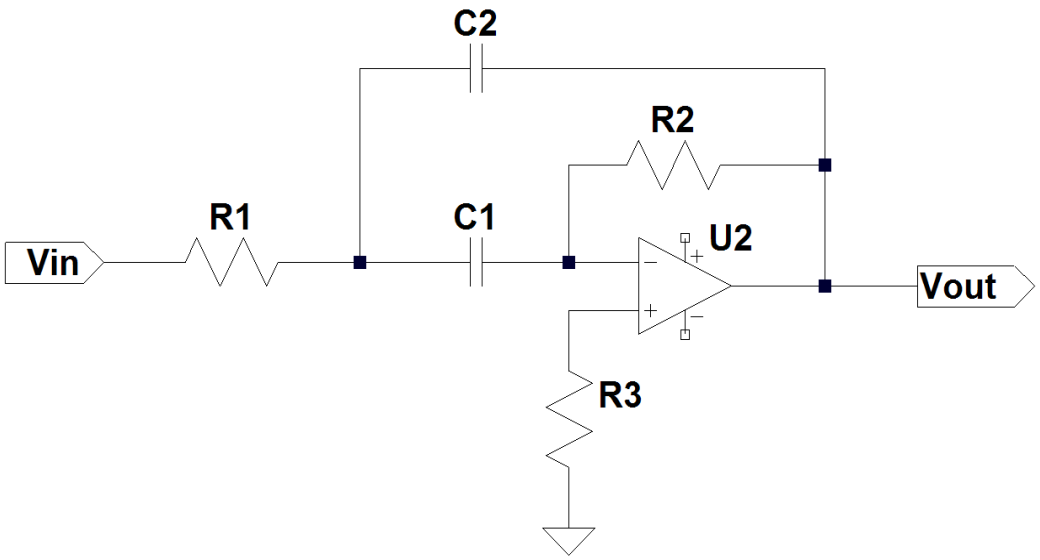

Figure 30: Delyiannis-Friend Band-Pass Filter

The mathematical representation of the band-pass filter is given in equation (43). Its cutoff frequency is given in equation (54) and by using this equation, the values for resistors (R_1 , R_2) and capacitors (C_1 , C_2) can be calculated. The resistors value is taken to be $R_1 = 10k\Omega$, $R_2 = 75k$ and after calculating the capacitors value it come out to be $C_1 = C_2 = 125\,pF$. The DC offset resistor R_3 is set to be equal to the input impedance of the negative input of the operational amplifier; $R_3 = 10k\Omega$.

To verify that the above values are chosen correctly and filter operates properly, its frequency response, obtained from a circuit simulation, is compared to the frequency response of the low-pass filter from equation (43) simulated in Matlab

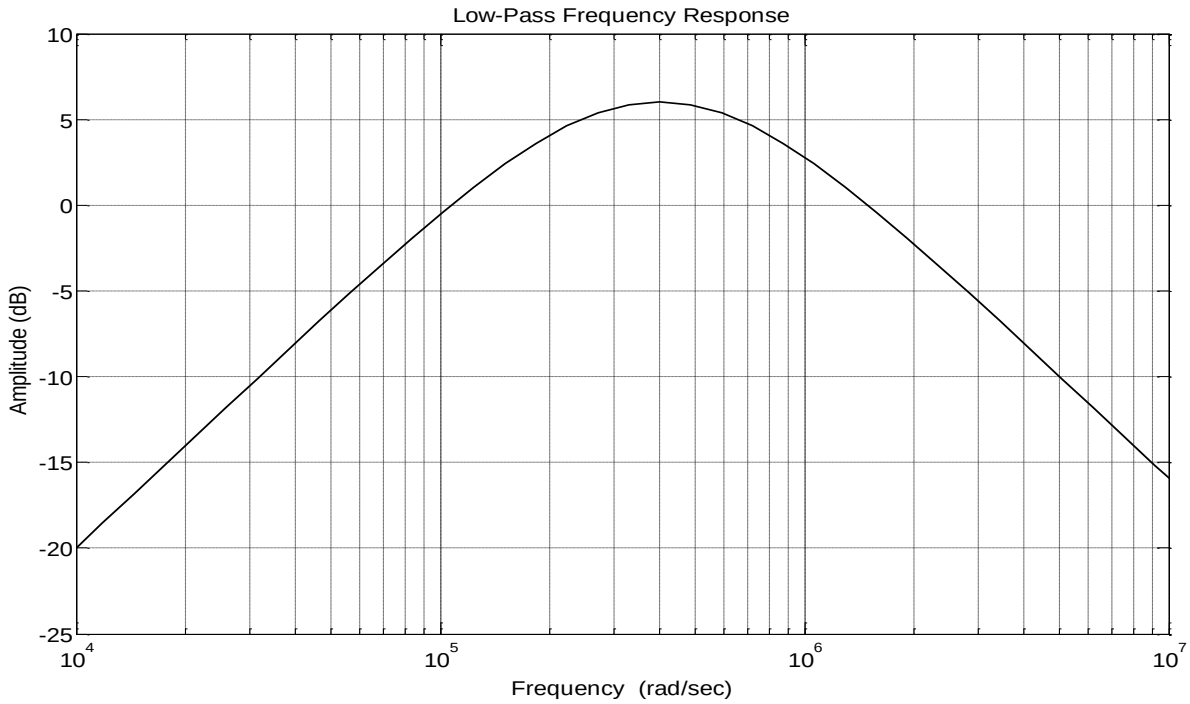

Figure 31: Frequency Response of a Band-Pass Filter using Matlab

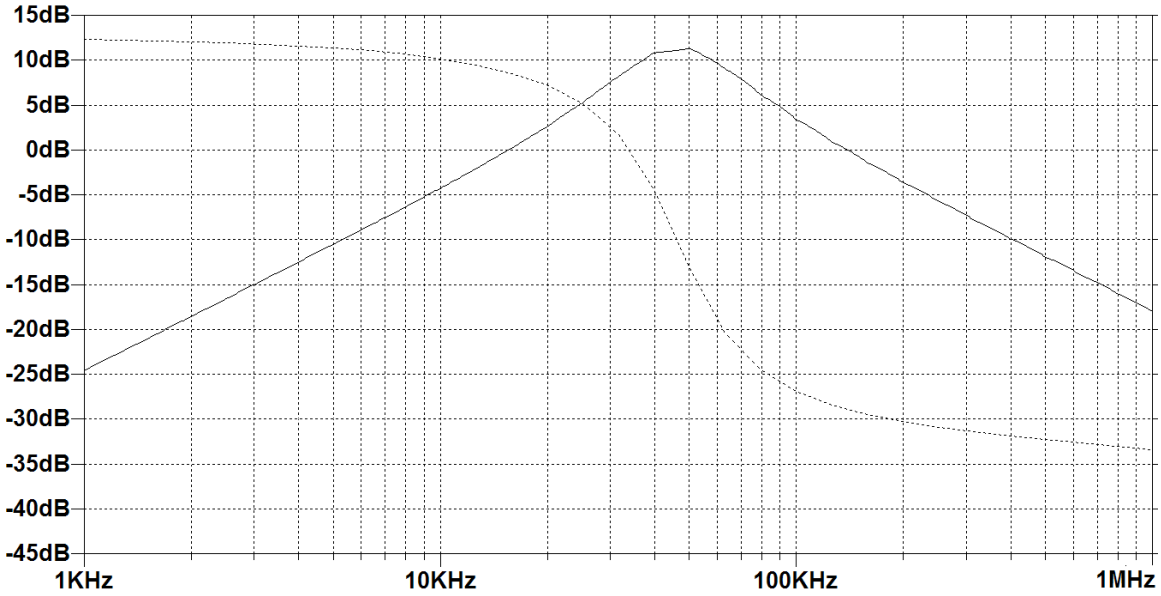

Figure 32: Frequency Response of a Band-Pass Filter using LTSpice

The constructed circuit exhibits the same frequency response as the theoretical estimation. The operating frequency of the gyroscope is located within the differentiation region of the filter, however, the high frequency region, unlike high-pass filter, is attenuated at the rate of -20 dB/decade. In order to observe the filter response in time domain, it is simulated with the same sinusoidal as with the above two filters

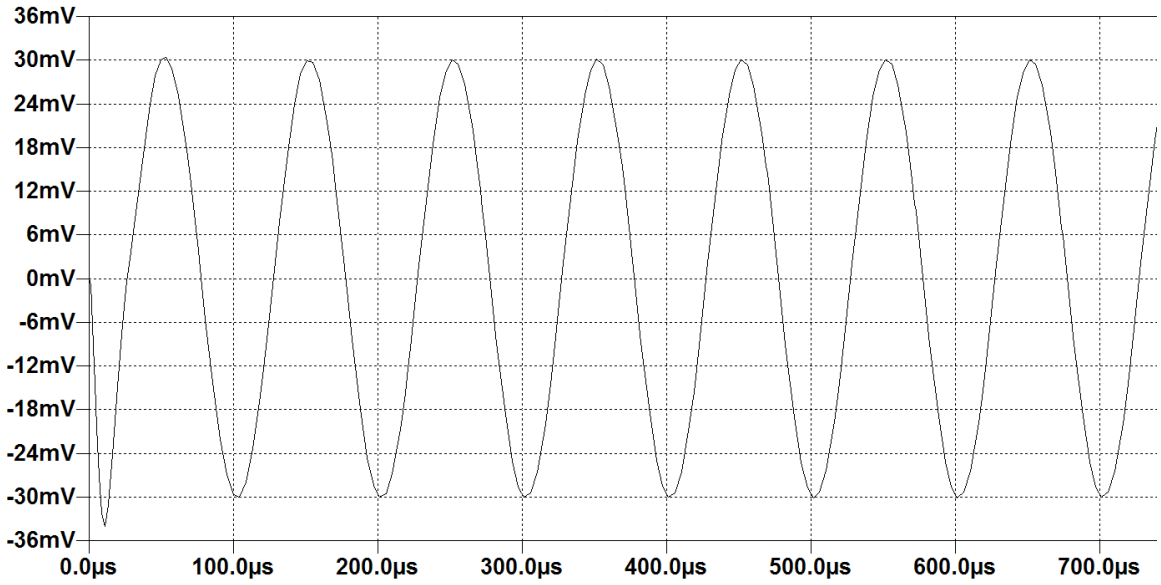

Figure 33: Response of a Band-Pass Filter in Time Domain

The amplitude of the output of the band-pass filter is higher than the one of the high-pass, which is something that should be expected. The band-pass filter is essentially acting as a first derivative and, therefore, the rate of differentiation is +20dB/decade. On the other hand, the high pass filter is acting as a second derivative and, therefore, it has a higher rate of differentiation that is +40dB/decade. The differentiation region, that includes the gyroscope operating point, ends at the cutoff frequency of the band-pass filter, which also ensures stability.

From above results, it is evident that all three filters have the same frequency and time responses in both Matlab and LTSpice simulations. Taking into account that during implementation the hardware might not respond exactly as predicted in simulations, the component values calculated above are not necessarily set in stone. The following chapter will show how above simulation results are translated into hardware results to produce purely analog advanced controller to control and estimate the rotation rate of the vibrating beam gyroscope.

CHAPTER IV

HARDWARE IMPLEMENTATION RESULTS

Active Disturbance Rejection Controller, simulated in Chapter III, was implemented, using pure analog circuit, and tested on the vibrating beam gyroscope system. The following sections describe in details the hardware set up, implementation of driving circuitry, implementation of sensing circuitry, implementation of signal conditioning and rotation rate estimation circuits and some of the implementation issues.

4.1 Experimental Set-Up

The ADRC control system was implemented on the Vibrating Beam Gyroscope.

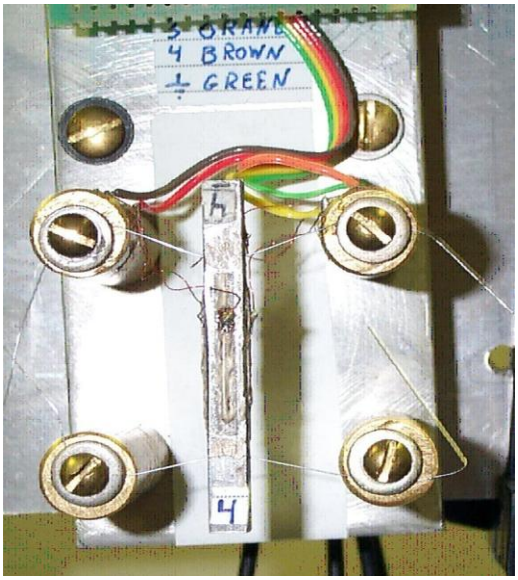

Figure 34: Vibrating Beam Gyroscope

Vibrating Beam Gyroscope consists of a 40 centimeter rectangular beam with piezoelectric material (PZT) attached to all four sides of the beam. The piezoelectric material is able to act as an actuator or a sensor, depending upon the polarity of the applied voltage. From Figure 34, the piezoelectric material on the front and back of the beam represent the actuation and sensing mode of the drive axis. The piezoelectric material on the right and left sides of the beam represent the actuation and sensing mode of the sense axis. The Z-Axis or the axis of rotation is going through top and bottom of the beam with the entire structure rotating around it.

To simulate rotation the Numark TTX direct drive turn table was used

Figure 35: Numark TTX Direct Drive Turn Table

The turn table has three constant speeds setting of 33.3, 45 and 78 RPM and a $\pm 50\,\%$ Velocity change slider. Therefore, the maximum range of rotation is from 0 RPM to 117 RPM in clockwise and counter-clockwise directions.

To simulate the input rotation rate signal, the gyroscope is place on top of the turn table. During integration it is important to make sure that the center of the beam, looking from the top, is right above the center of the turn table. After the integration and wiring the system set-up is

Figure 36: Turn Table with Vibrating Beam Gyroscope

The gyroscope signal wires were connected to the ADRC controller and rotation rate approximation circuitry. Depending on the speed setting, each iteration was tested for 30 to 60 seconds, to capture both, the transient and the steady state of rotation rate approximation response. The following chapters describe the controller and rotation rate approximation hardware results.

4.2 Analog Circuit Implementation

Combining the theoretical derivations and simulation results presented so far, the analog hardware implementation of ADRC on drive and sense axis is presented next. Main issues of analog ADRC implementation and rotation rate approximation technique are also included.

4.2.1 Driving and Sensing Mode Implementation

The driving and sensing mode control loops of Figure 12 and 13 were implemented using the simulated circuits from Chapters III and IV. The circuits were constructed on a bread board for verification purposes and then designed using a layout EAGLE CAD tool

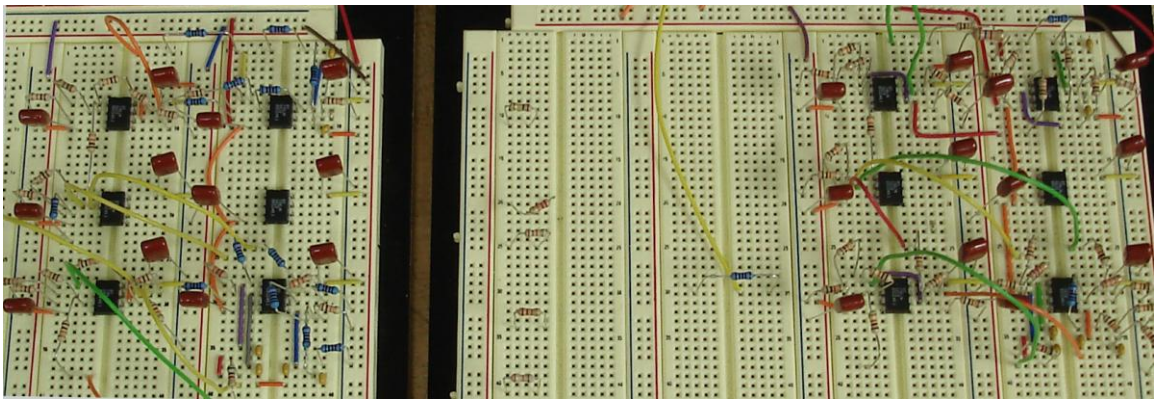

Figure 37: Drive and Sense Axis ADRC Bread Board

During implementation, there were two main issues with analog ADRC design: Signal integrity and the noise induced during operation. Signal integrity effects response

time of the system as well as systems accuracy. Since the entire design is done using active analog circuitry and the signals are in kHz range, it is important to make sure that the components, like operational amplifiers, do not introduce lags or phase delays and become limiting factors in the system. In order to avoid that, the high slew rate and high bandwidth Analog Device AD746 operational amplifier was chosen for the design. Its slew rate is $75V/\mu s$ and the operational bandwidth is 13 MHz, which means that the signal is essentially passing through the amplifier instantaneously and its bandwidth is well within the bandwidth of the operational amplifier. On the other hand, system accuracy depends on both controller design and components used to realize the design. One important design requirement of analog ADRC is that intermediate signals must not be saturated. For example, if at least one signal produced by a controller and especially control signal is saturated (could be the output of a filter or a control signal), then the tracking accuracy is greatly degraded. In this case the signal saturation simply means the loss of the information in a control loop, which leads to the error in a process of rotation rate approximation. By choosing high tolerance, high operational voltage and bandwidth components in combination with good and accurate analog circuit design, these issues can be avoided.

The introduction of noise during implementation is an inevitable issue that any system has. The noise can come from many different sources, such as bread board (since the initial design is done using a bread board), long wires with high speed signals going through them, poor circuit design and low tolerance components, poorly tuned controller, e.t.c. To eliminate most of these issues, we transformed bread board design to a next level by designing and ordering a Printed Circuit Board (PCB). PCB in combination with the

accurate circuit design and choosing high tolerance components provided a huge boost in performance and help creating low noise system.

The following figures represent the hardware results produced by an analog ADRC controller implemented for a vibrating beam gyroscope. The Hewllet Packard signal generator was used as a reference signal source producing a sinusoidal at 10kHz with an amplitude of $\pm 100mV$. The circuit is powered up using Hewllet Packard bipolar DC voltage source at $\pm 16V$ for maximum operational amplifier performance possibility. The first hardware results is the input and output of the Drive Axis shown in Figure 38

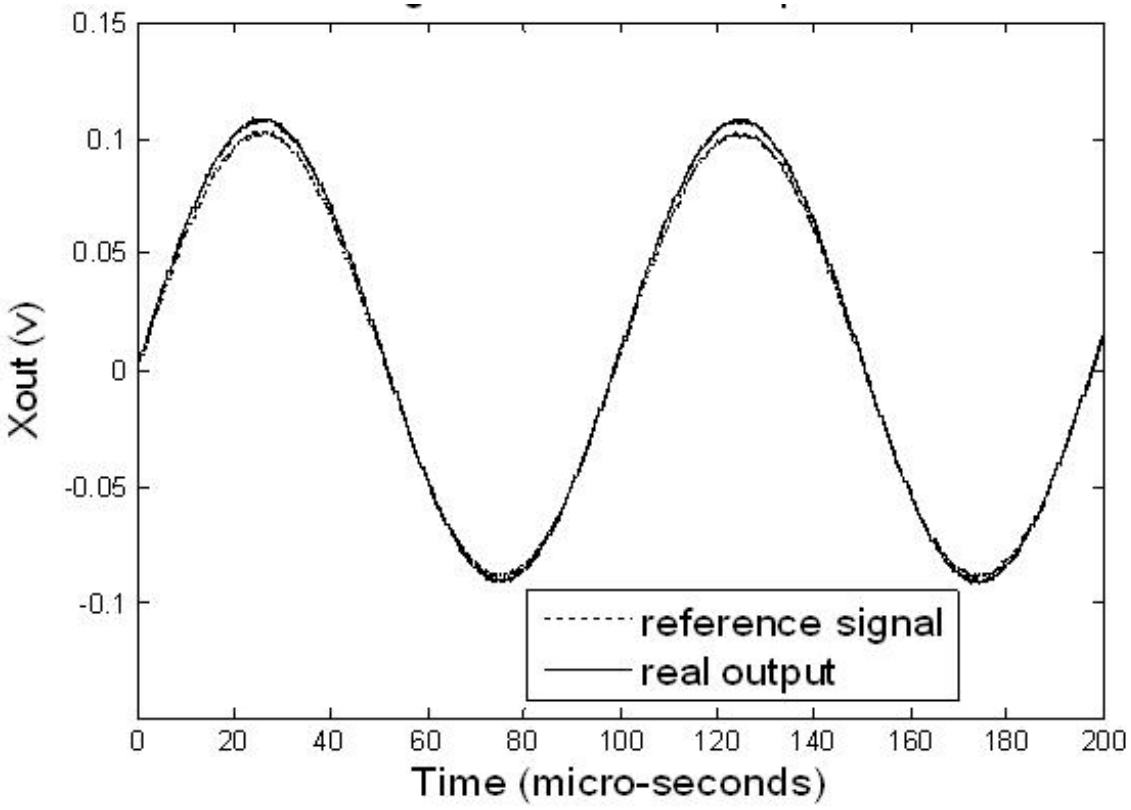

Figure 38: Input and Output of Drive Axis

From Figure 38, the output of Drive Axis is almost identical to the desired reference input signal, with amplitude being constant at $\pm 100mV$ and frequency being

the resonant frequency of the drive axis $\omega_x = 10.1kHz$. To see how fast the drive axis output reaches its steady state, the snap shot of the transient response was taken

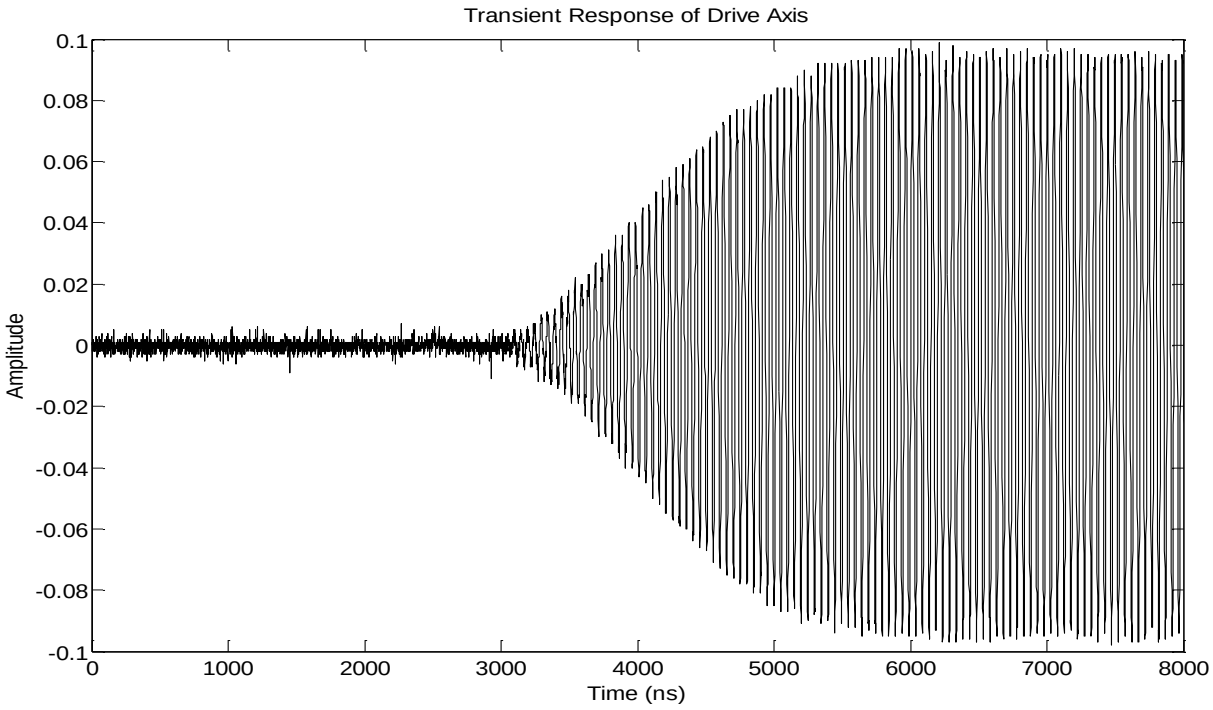

Figure 39: Transient Response of Drive Axis

From Figure 39, the response time of the drive axis output can be approximated to be $\approx 3\mu s$. Such high performance is one of the main features of the analog ADRC implementation for this design.

As it was mentioned above, it is important to make sure that the control signal of drive axis is not saturated. The next figure shows the control signal of the drive axis

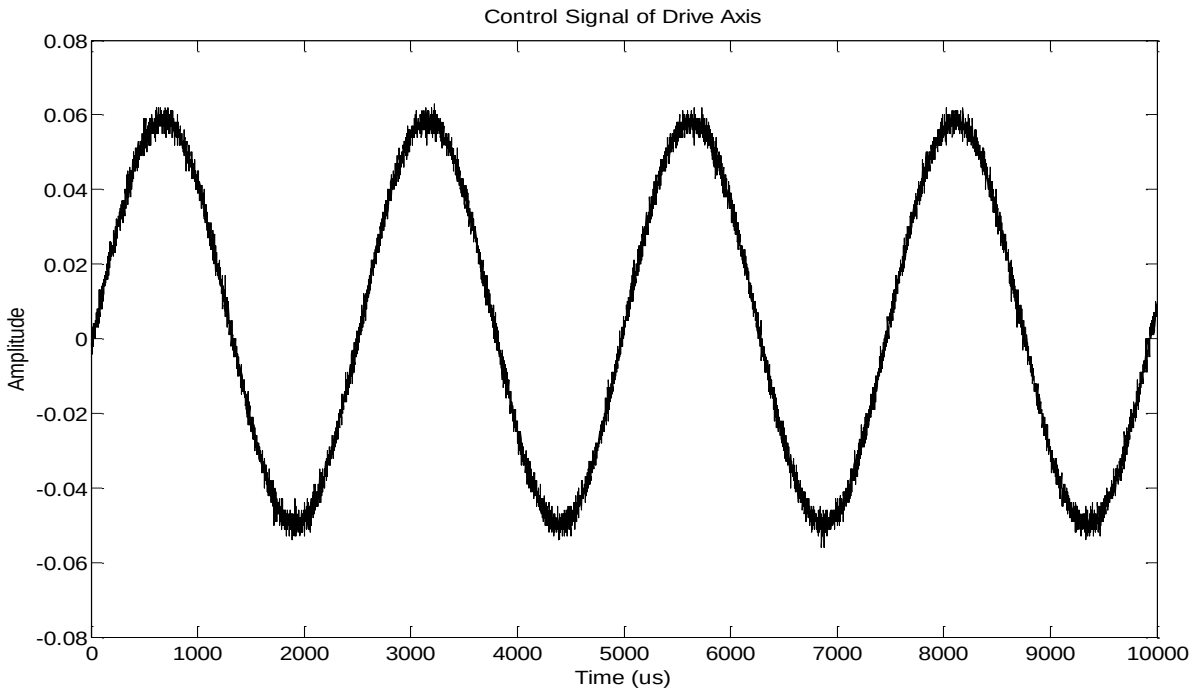

Figure 40: Control Signal of Drive Axis

From Figure 40 it is evident that the control signal of drive axis is a sinusoidal with constant amplitude and frequency.

The next figures represent the hardware results of sense axis produced by an analog ADRC controller implemented for a vibrating beam gyroscope. The Hewllet Packard signal generator was used as a reference signal source producing a constant zero volts signal. The circuit is powered up using Hewllet Packard bipolar DC voltage source at $\pm 16V$ for maximum operational amplifier performance possibility.

The first figure shows the output signal of the sense axis

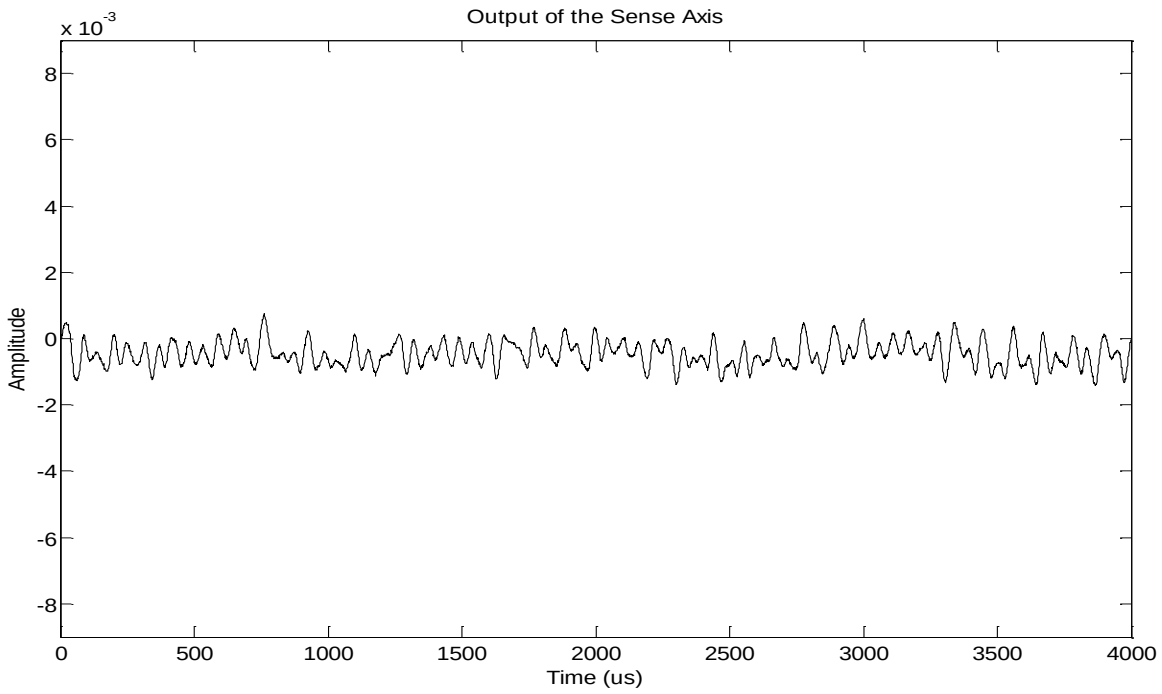

Figure 41: Output of Sense Axis

From Figure 41, the output of sense axis can be considered to be zero. The vibration is the signal represents the small high frequency noise added to a signal. The average amplitude of the noise is approximately $1-3\mu V$, therefore, the output of sense axis for purposes of this project can be considered to be zero. Since the output of sense axis does not have to "reach" any particular value other then zero, its transient time can be considered to be zero, since it was impossible to determine. On the other hand, making sure that the control signal of the sense axis is not saturated is very important, since it contain the rotation rate information. Next figure shows the control signal of sense axis

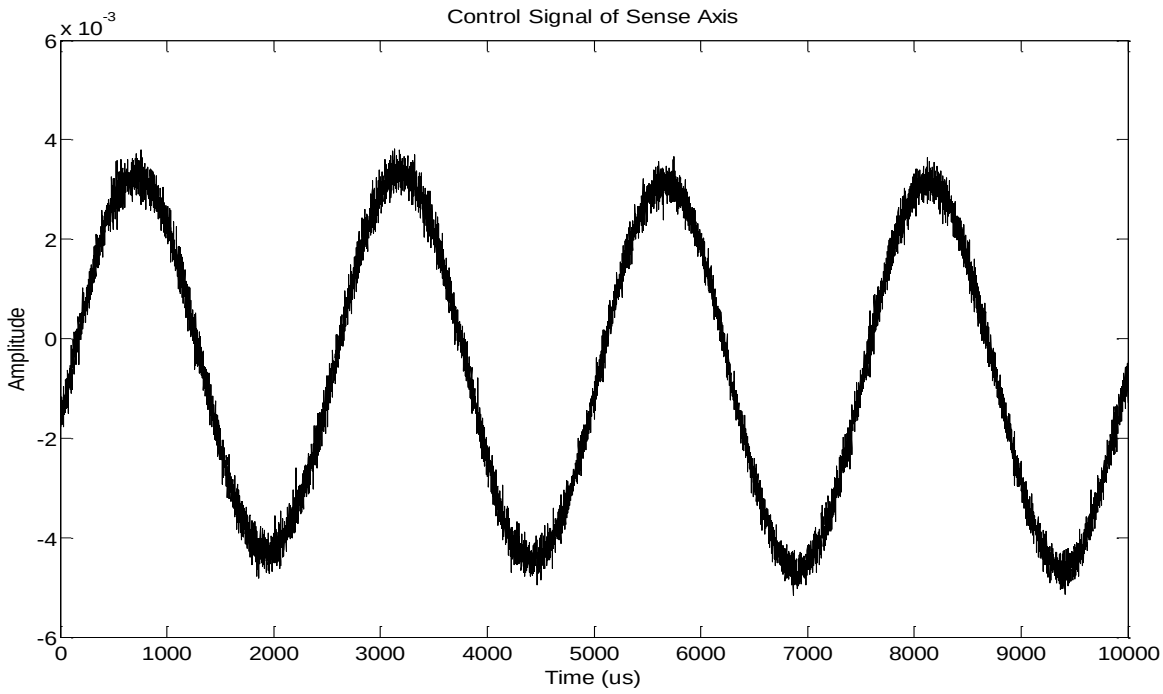

Figure 42: Control Signal of Sense Axis

Figure 42 shows a control signal of sense axis that is a sinusoidal and is not saturated. Although the amplitude of the control signal is relatively small, during rotation rate approximation, it can be easily amplified for further processing. Also, from Figure 42 it is shown that the response contains a small DC bias. The DC bias exist in the output since the response is a combination of sinusoidal signals and since they are multiplied, the small DC bias is a portion of the result. It is undesirable feature and, therefore, will be eliminated in a signal processing stage of the design.

The following subsection will in details describe the design of the signal conditioning and demodulation portion of the sensor development.

4.2.2 Signal Conditioning and Demodulation Circuit Hardware Results

The final part of the Vibrating Beam Gyroscope design is to be able to correctly approximate rotation rate. As it was mentioned above, in order to achieve that the control signal of the sense axis is demodulated and then processed to obtain the rotation rate. In Chpater II the mathematical derivation was performed and by combining equations 9 through 13, a simple block diagram of rotation rate approximation process is obtained

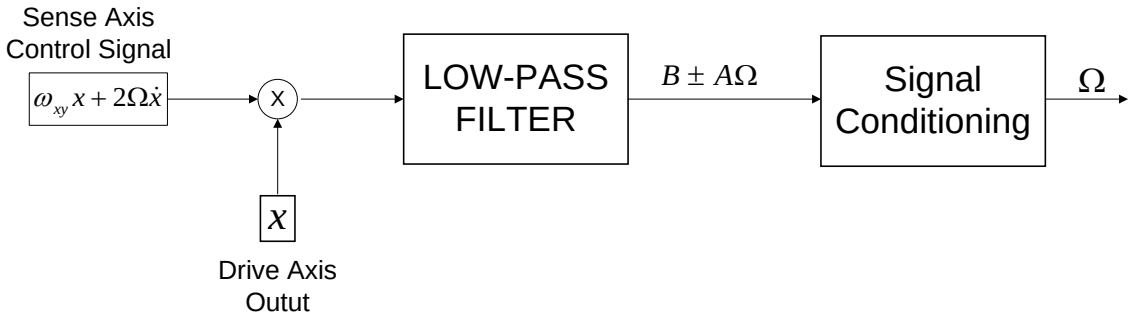

Figure 43: Rotation Rate Approximation Block Diagram

The block diagram of Figure 43 can be broken into three parts during implementation: multiplication, low-pass filtering, and signal conditioning. To verify that each part is operating properly, each circuit is designed and verified separately and then all three circuits are integrated together.

In order to multiply two analog signals, AD633 analog multiplier chip was used. The reason for choosing this particular multiplier is that it has a wide operating range and contains internal division circuit, which attenuates multiplication result ten times. This feature is very important, since it allows larger signals to be multiplied without getting

into saturation. At the same time, this feature is undesirable since the resulting signal is ten times smaller than what's expected. Hence, ten times amplification is required during signal conditioning to obtain correct results.

The low-pass filter design is exactly the same as the one for the controller, except for the cutoff frequency

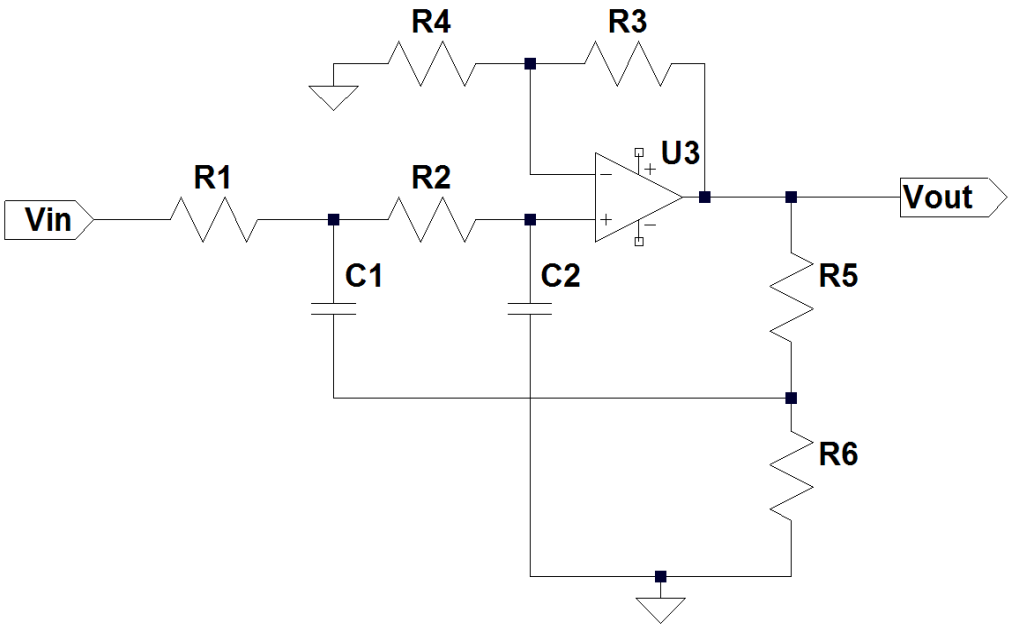

Figure 44: Low-Pass Filter for Demodulation Circuit

From equation (13), the low pass filter has to filter out first two terms and leave the remaining rotation rate signal. The frequency of the first two terms is $2\omega_x = 20.2kHz$. The accepted rule of thumb is that the cutoff frequency of the low-pass filter should be approximately a decade below the frequency it is trying to filter out. With this in mind the cutoff frequency of the filter was chosen to be 500Hz. To achieve that, the circuit parameters are chosen to be

$$R_1 = R_2 = 10kHz, \quad C_1 = C_2 = 31.8nF \tag{59}$$

The frequency response of the filter is as shown below

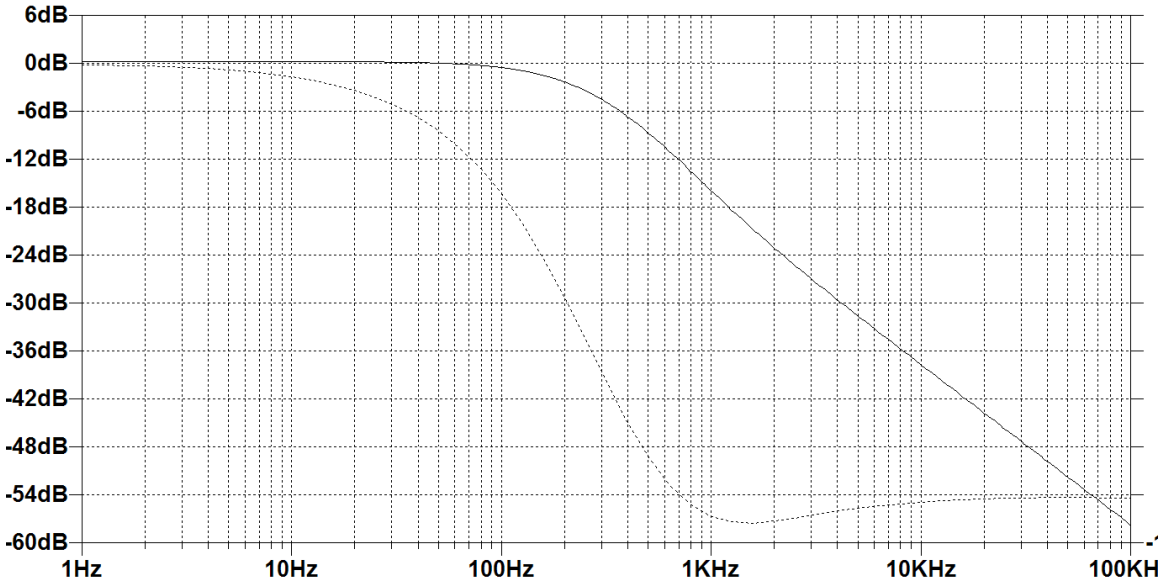

Figure 45: Frequency Response of the Demodulation LPF

The frequency response shows that the filter provides a little bit over 40 dB of attenuation at 20 kHz, which should be sufficient to eliminate double frequency components of equation (13). To proof the correctness of the claim, the circuit is simulated with a sinusoidal signal at 20 kHz frequency

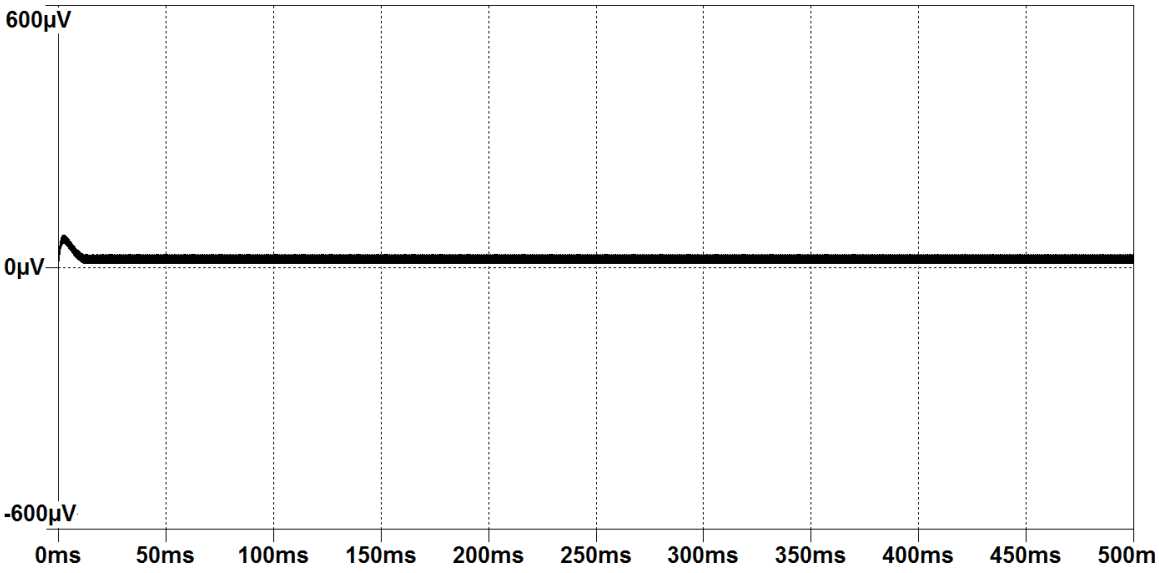

Figure 46: Time Response of the Demodulation LPF

Figure 46 shows how low-pass filter eliminates the double frequency components from equation (13), leaving only a nano-volts DC bias that can be considered to be zero.

The last part of the design is elimination of the DC bias and gains that were added to the rotation rate signal during demodulation process. In order to achieve that, the op-amp gain circuit of Figure 8 is designed with addition of an input capacitor. The value for a capacitor is purposely chosen to be larger, so it only acts as a DC blocking component.

After integrating all of the circuits discussed in the previous two chapters, the system was tested with the turn table. The input speed was in the range of 0 to 117 RPM resulting in 22 different set points. The relationship between the input rotation rate and the output voltage is crucial, since it determines the calibration curve for determining rotation rates other than the tested set points. The plot of input rotation rate versus the measured voltage is

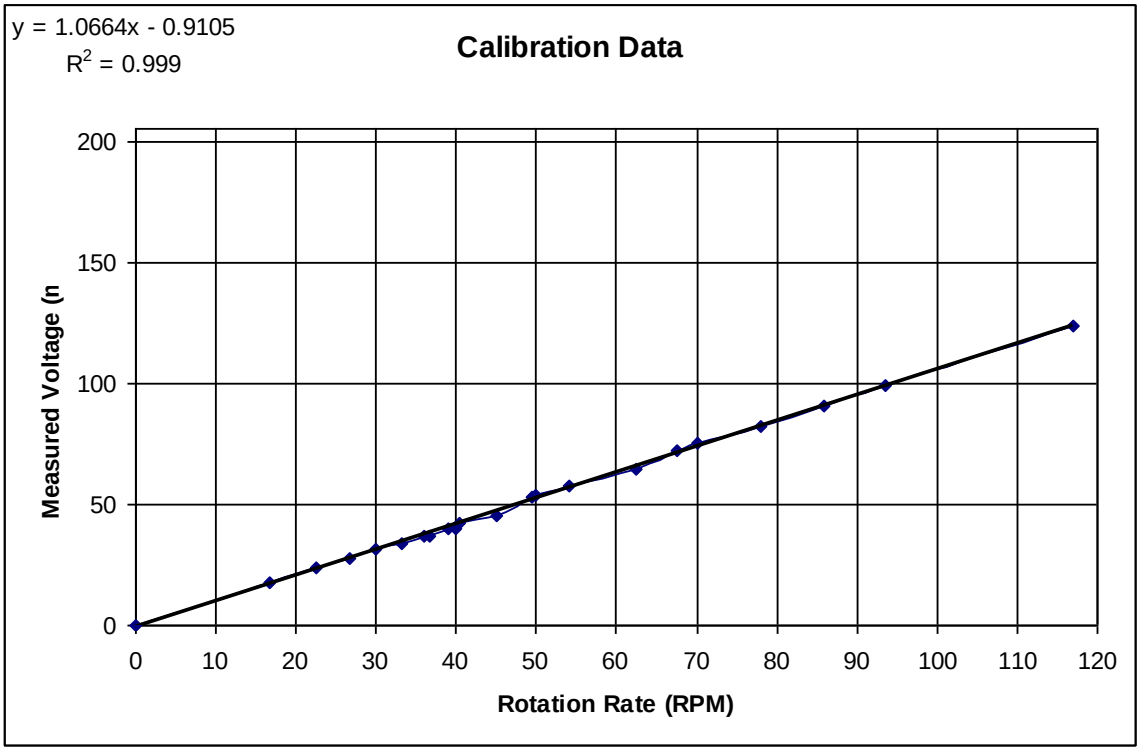

Figure 47: Rotation Rate vs Measured Voltage

Following figures show the measured voltage of a certain rotation rate input. The first figure is the measured voltage with rotation rate of 0 RPM

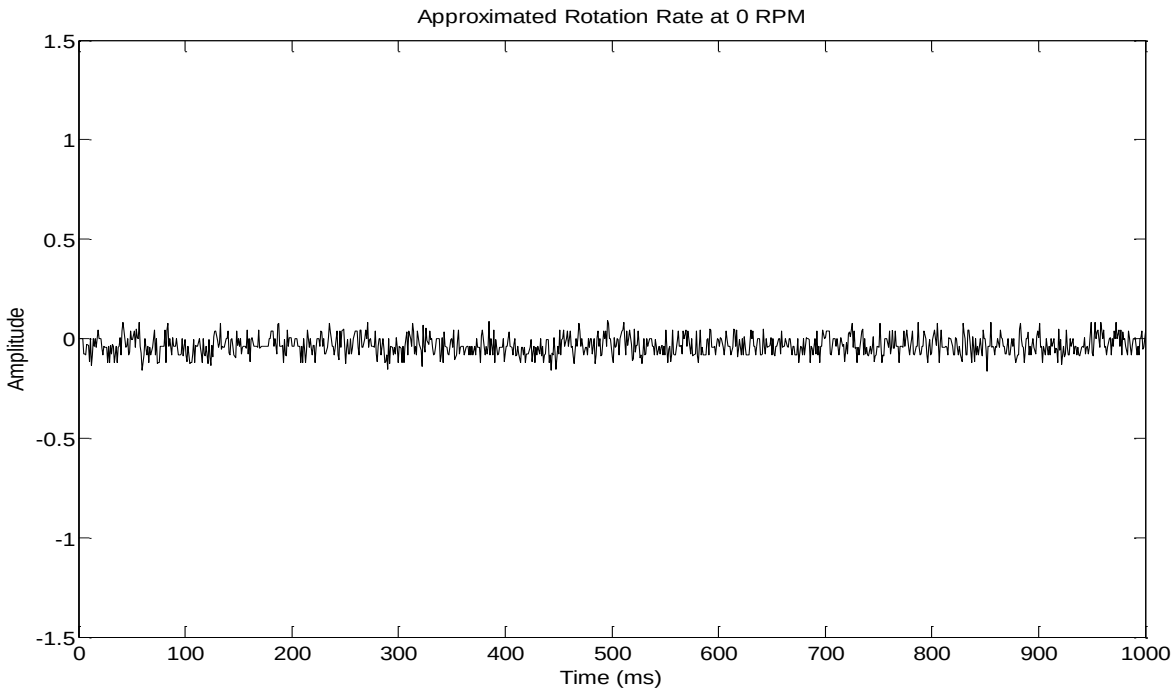

Figure 48: Measured Voltage at 0 RPM

Next, the rotation rate was set to 16.7 RPM

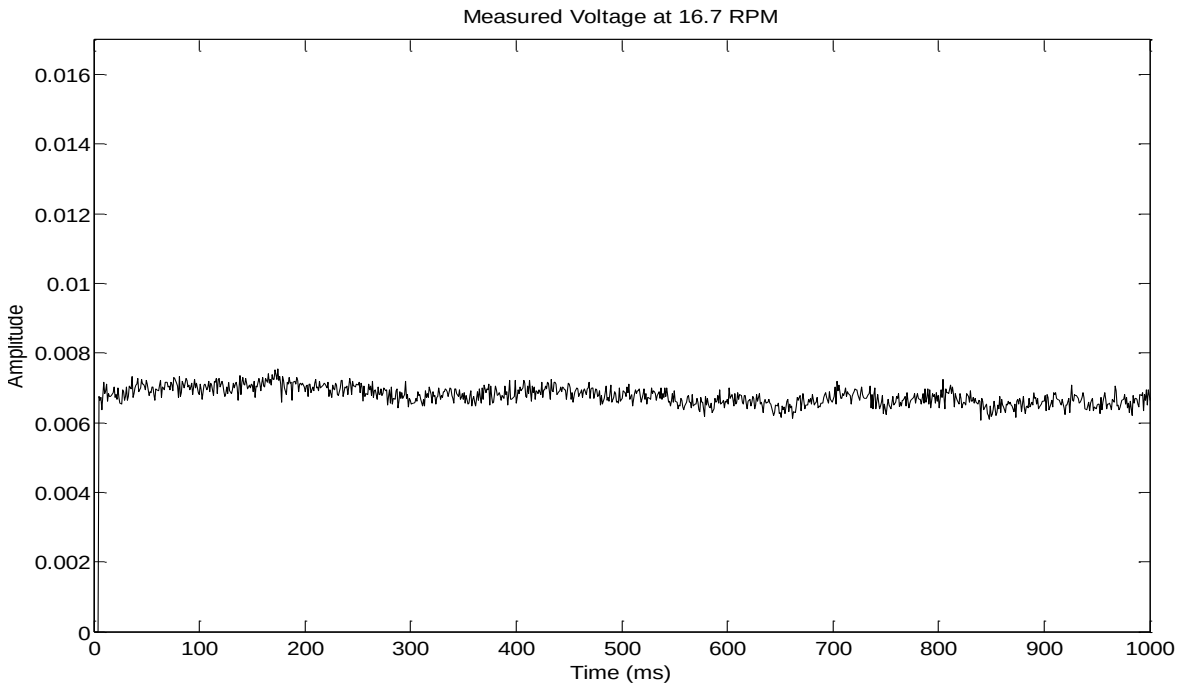

Figure 49: Measured Voltage at 16.7 RPM

Next figure is the measured voltage at 33.3 RPM

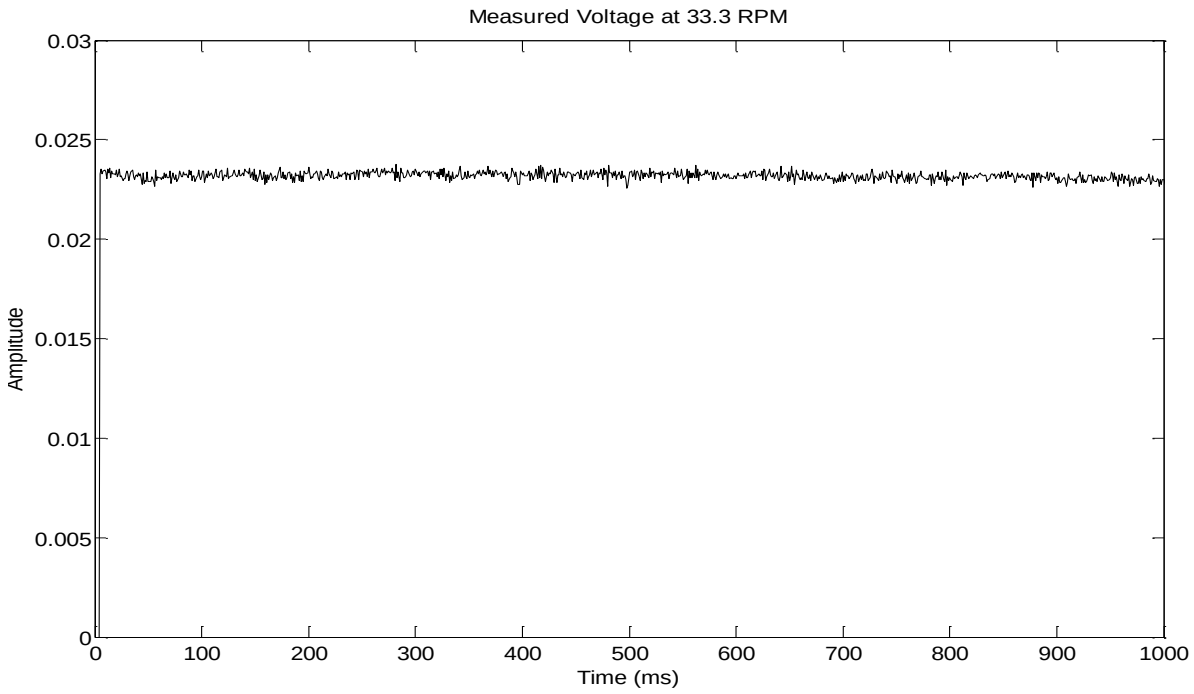

Figure 50: Measured Voltage at 33.3 RPM

Next figure is the measured voltage at 50 RPM

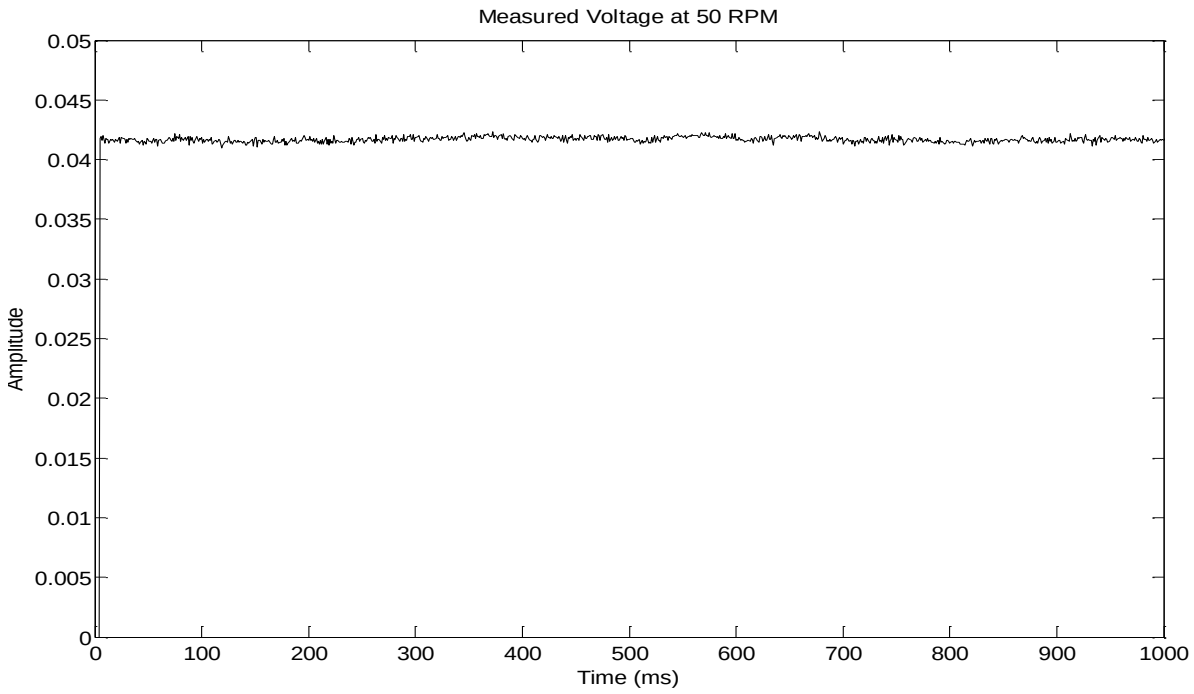

Figure 51: Measured Voltage at 50 RPM

All three figures show a very fast response to the rotation rate input and it is approximately equal to $10\mu s$. The fast response time is one of the main features of this design and is a main attribute of high-performance.

The other important feature is that the relationship between rotation rate and the measured voltage is very linear resulting in the linear equation

$$y = 1.0664x - 0.9105 \tag{60}$$

These results are extremely positive and lead to the following conclusions. The sensor was able to successfully approximate rotation rate up to 117 RPM. The only reason measurement of higher RPM were not tested is because the maximum speed of the turn table is 117 RPM. This means that in order to determine the maximum rotation rate that this sensor can sense is unknown and yet to be determined with more sophisticated

hardware test set-up. Knowing the limits of the sensor allows us to compare current design with existing products in industry. The results that are presented in Figure 47 are already better than the existing MEMS gyroscope from companies like Analog Device. The gyroscope from Analog Device (ADXR300) can sense rotation rate up to 50 RPM with response time of 35 ms, but it essentially operates in open loop. The vibrating beam gyroscope controlled by an analog ADRC has response time of $10us$ with ability to sense rotation rate up to 117 RPM, so far.

On the other hand, the measured voltage has a very linear relationship with input rotation rate. This means that the addition of a closed loop control system minimizes the drift and other nonlinearities that are generally big issues in MEMS gyroscope industry. Linear relationship allows us to design and build a very simple Graphical User Interface (GUI) for further processing and use depending on the application. For example, for purposes of demonstration, equation (60) was programmed into a dsPIC micro-processor, which in turn was interfaced with an LCD display. Hence, during testing the rotation rate could be seen as a number as oppose to waveform on the oscilloscope. However, for more sophisticated applications, the rotation rate signal (or equation (60)) becomes a control signal of an actuator for particular operation or a feedback for a bigger system.

Next chapter provides concluding remarks and will talk about future work.

CHAPTER VII

CONCLUSION

The purpose of this research was to develop a high-performance and low-cost MEMS gyroscope using advanced closed loop control system. By designing and implementing analog ADRC both above requirements were satisfied. Analog ADRC provides the fastest response time possible (because the circuit is analog), eliminates both internal and external disturbances, and increases the bandwidth of the gyroscope beyond its natural frequency; all of these features constitute to high-performance. On the other hand, the overall design is extremely economical, given that the entire design is done using pure active and passive analog components. The prototype of the entire system was only $28 and it's only because the components were not purchased at production quantities. However, ones the design is fully integrated on the same silicon wafer as the mechanical structure and batch fabricated in a clean room, the cost reduction should be expected to be 3 to 4 times.

As it was mentioned before, the purpose of this work is to develop a product with novel technology for a broad range of applications. Achieving such a goal requires a set

of steps that need to be followed to make sure that the overall resulting product is fully available for the market. Fortunately, National Aeronautics and Space Administration (NASA) has developed so called Technology Readiness Level (TRL), which is a measure used by US government agencies and many companies world wide to assess the maturity of the technology. When a new technology is first invented it is generally not suitable for immediate application, instead it goes through extensive experimentation, refinement and testing. TRL helps the new technology to get to a new level, which is to be incorporate to a system or a large subsystem for an industrial application. The following table shows the nine steps of TRL

TABLE I: TECHNOLOGY READINESS LEVEL

Technology Readiness Level	Description
1. Basic principles observed and reported	Lowest level of technology readiness. Scientific research begins to be translated into applied research and development. Example might include paper studies of a technology's basic properties.
2. Technology concept and/or application formulated	Invention begins. Once basic principles are observed, practical applications can be invented. The application is speculative and there is no proof or detailed analysis to support the assumption. Examples are still limited to paper studies.
3. Analytical and experimental critical function and/or characteristic proof of concept	Active research and development is initiated. This includes analytical studies and laboratory studies to physically validate analytical predictions of separate elements of the technology. Examples include components that are not yet integrated or representative.

4. Component and/or breadboard validation in laboratory environment	Basic technological components are integrated to establish that the pieces will work together. This is relatively "low fidelity" compared to the eventual system. Examples include integration of 'ad hoc' hardware in a laboratory.
5. Component and/or breadboard validation in relevant environment	Fidelity of breadboard technology increases significantly. The basic technological components are integrated with reasonably realistic supporting elements so that the technology can be tested in a simulated environment. Examples include 'high fidelity' laboratory integration of components.
6. System/subsystem model or prototype demonstration in a relevant environment	Representative model or prototype system, which is well beyond the breadboard tested for TRL 5, is tested in a relevant environment. Represents a major step up in a technology's demonstrated readiness. Examples include testing a prototype in a high fidelity laboratory environment or in simulated operational environment.
7. System prototype demonstration in an operational environment	Prototype near or at planned operational system. Represents a major step up from TRL 6, requiring the demonstration of an actual system prototype in an operational environment, such as in an aircraft, vehicle or space. Examples include testing the prototype in a test bed aircraft.
8. Actual system completed and 'flight qualified' through test and demonstration	Technology has been proven to work in its final form and under expected conditions. In almost all cases, this TRL represents the end of true system development. Examples include developmental test and evaluation of the system in its intended weapon system to determine if it meets design specifications.
9. Actual system 'flight proven' through successful mission operations	Actual application of the technology in its final form and under mission conditions, such as those encountered in operational test and evaluation. In almost all cases, this is the end of the last "bug fixing" aspects of true system development. Examples include using the system under operational mission conditions.

Next, we show how following the TRL steps lead us to very promising results, starting with step one. In step one the application of advanced controller for VBG gyroscope was started with an extensive literature review in both ADRC and MEMS gyroscopes areas. In step two, the literature review led to an understanding and formulation of a problem that MEMS industry currently faces as well as understanding the main application where a new product can be successfully used. In step three, the ADRC was reformulated and transferred into transfer function representation for analog implementation. Extensive simulations proved the theoretical claims and prepared the controller and the system to be integrated using hardware. In step four each part of the ADRC controller was designed and bread-boarded to make sure that the simulation results correspond to hardware results. In step five the advanced controller was fully integrated together with the VBG gyroscope and test set-up hardware was build for extensive testing. In step six, the integrated hardware of TRL5 is tested using turn table in the laboratory environment to proof that the simulation result directly correspond to the experimental ones.

Although this work has been completed up to step six, achieving this level provides a major step up in a technology readiness. Starting from step seven up to step nine would definitely require an industry partner to be able to complete them. The industry partner would provide the financial means as well as an application.

This work, besides achieving high-performance and providing low-cost solution, furnishes two novel designs concepts. First, Active Disturbance Rejection Controller can now be build using pure analog circuit, which has never been done before. Second, it is the first time that the advanced controller has been successfully implemented in hardware

to control an inertial rate sensor like gyroscope. This work provides a novel solution to applications that require high-performance and low-cost inertial sensors.

7.1 Future Research and Work

The future work should include completion of the TRL steps shown in previous section. In order to achieve that, the first step is to find an industrial partner that would be able to help in development (mainly financial and equipment) of a Micro-Machined gyroscope. Once that's achieved the prototype of the ADRC should be build on a silicon wafer and packaged together with the MEMS gyroscope mechanical structure. The fully IC integrated and packaged MEMS gyroscope then can be tested. The series of tests should determine the operation limits, temperature limits, stability, withstand ability, immunity to large external disturbances and so forth. Once the tests are complete the device can be used in an actual application and then released for full production.

Another promising research path can be taken if analog ADRC is implemented for MEMS accelerometer. The problem with MEMS accelerometers is quite different, since they are already low-cost and are heavily mass-produced. Therefore, the research should be focused on finding a very specific application that requires a very high-performance, but simple design.

REFERENCES

1. Sungsu Park, Roberto Horowitz, "Adaptive Control for the Conventional Mode of Operation of MEMS Gyroscopes," Journal of Microelectromechanical Systems, vol.12, NO. 1, February 2003.

2. P. B. Ljung, "Micromachined Gyroscope with Integrated Electronics," Doctoral Dissertation, Berkeley, Ca, 1997.

3. S. Chang, M. Chia, P. Castillo-Borelley, W. Higdon, Q. Jiang, J. Johnson, L. Obedier, M. Putty, Q Shi, D. Sporks, S. Zarabadi, "An electroformed CMOS Integrated Rate Sensor," Sensors and Actuators, vol. A 66, pp. 138-143, 1998.

4. X. Jiang, J. Seeger, M Kraft, B. E. Boser, "A Monolithic Surface Micromachined Z-Axis Gyroscope with Digital Output," in Proc. IEEE 2000 symp. VLSI Circuits, Honolulu, HI, pp. 16-19, June 2000.

5. P. W. Loveday, C. A Rogers, "Modification of Piezoelectric Vibratory Gyroscope Resonator Parameters by Feedback Control," IEEE Transactions on ultrasonics and Ferroelectrics.

6. C. Painter, A. Shkel, " Active Structural Error Supression in MEMS Vibratory Rate Integrating Gyroscopes," IEEE Sensors Journal, vol 3. NO 5, October 2003.

7. S. Park, R. Horowitz, "Discrete Time Adaptive Control for a MEMS Gyroscope," International Journal of Adaptive Control and Signal Processing, 2005.

8. C. Acar, S. Eler, A. Shkel, "Concept, Implementation and Control of Wide Bandwidth MEMS Gyroscope," Proceed. ACC, Arlington, VA, June 25-27, 2001.

9. A. Shkel, R. Horowitz, A. A. Seshia, S. Park, R. Howe, "Dynamics and Control of Micromachined Gyroscopes," Proceed. ACC, San Diego, CA, June 1999.

10. B. Borovic, A. Q. Liu, D. Popa, H. Cai, F. L. Lewis, "Open Loop Versus Closed Loop Control of MEMS Devices: Choices and Issues," Journal Microengineering, pp. 1917-1924, 2005.

11. R. Oboe, R. Antonello, E. Lasalandra, G. S. Durante, L. Prandi, "Control of a Z-Axis MEMS Vibrational Gyroscope, " IEEE/ASME Transactions on Mechatronics, vol. 10, NO 4, August 2005.

12. Z. Gao, "Scaling and Bandwidth-Parametrization Based Controller-Tuning," Dept. of Electrical and computer Engineering, Cleveland State University.

13. R. Miklosovic, Z. Gao, “A Dynamic Decoupling Method for Controlling High-Performance Turbofan Engines,” Center of Advanced Control Technologies, Cleveland State University.

14. Q. Zheng, L. Dong, Z. Gao, “Control and Time-Varying Rotation Rate Estimation of Vibrational MEMS Gyroscopes”, Instrumental, Control and Electronics Consortium.

15. R. Miklosovic, Z. Gao, “A Robust Two Degree of Freedom Control design Technique and its Practical Application,” Department of Electrical and computer Engineering, Cleveland State University.

16. A. Radke, Z. Gao, “A survey of State and disturbance Observers for Practitioners,” Center of Advanced Control Technologies, Cleveland State University.

17. Z. Gao, “ADRC: A Paradigm Shift in feedback control System Design,” Center of Advanced Control Technologies, Cleveland State University.

18. Q. Zheng, L. Gao, Z. Gao, “Estimation of Plant Dynamics and Disturbance from Input-Output Data in Real-Time,” Center of Advanced Control Technologies, Cleveland State University.

19. R. Miklosovic, A. Radke, Z. Gao, “Discrete Implementation and Generalization of the Extended State Observer,” Center of Advanced control Technology, Cleveland State University.

20. G. Tian, Z. Gao, “Frequency Response Analysis of ADRC Based Control System” Center of Advanced Control Technologies, Cleveland State University.

21. Q. Zheng, Z. Gao, “Motion Control Design Optimazation: Problem and Solution” Center of Advanced Control Technologies, Cleveland State University.

22. Y. Hou, Z. Gao, F. Jiang, B. T. Boulter, “ADRC for Web Tension Regulation,” Cleveland State University.

23. W. A. Clark, “Micromachined Vibratory Gyroscope,” PhD Dissertation, The University of California Berkely, 1997.

24. A. Shkel, C. Acar, C. Palmer, “Two Types of Micromachined Vibratory Gyroscopes,” IEEE, 2005.

25. C. Acar, A. Shkel, “Nonresonant Micromachined Gyroscopes With Structural Mode-Decoupling,” IEEE Sensors Journal, vol. 3, NO 4, August 2003.

26. C. Acar, A. Shkel, “Four Degrees of Freedom Micromachined Gyroscopes,” Journal of Modeling and Simulation of Microsystems, vol. 2, NO. 1, pp. 71-82, 2001.

27. G. Kovacs, N. Maluf, K. Petersen, “Bulk Micromachining of Silicon,” Proceed. IEEE, vol. 86, NO. 8, August 1998.

28. C. Acar, A. Shkel, "Inherntly Robust Micromachined Gyroscopes with 2-DOF Sense –Mode Oscillator," Journal of Microelectromechanical Systems, vol. 15, NO. 2, April, 2006.

29. M. Weinberg, A. Kourepenis, "Error Sources in In-Plane Silicon Tuning Fork MEMS Gyroscope," Journal of Microelectromechanical Systems, vol. 15, NO. 3, June 2006.

30. F. Gretillat, M. A. Gretillat, N. F. de Rooij, "Improved Design of Silicon Micromachined Gyroscope with Piezoresistive Detection and Electromagnatic Excitation," IEEE Jouranl of Microelectromechanical Systems, vol. 8, NO. 3, September 1999.

31. G. He, C. Nguyen, J. Hui, S. Ricky-Lee, H. Loung, "Design and Analysis of a Mictogyroscope with Sol-Gel Piezoelectric Plate," Smart Mater. Struct. 1999.

32. R. Leland, "Mechanical-Thermal Noise in MEMS Gyroscopes," IEEE Sensors Journal, vol. 5, NO. 3, June 2005.

33. N. Yazdi, F. Ayazi, K. Najafi, "Micromachined Inertial Sensors," Proceed. IEEE, vol. 86, NO. 8, August 1998.

34. K. Petersen, "Silicon as a Mechanical Material," Proceed. IEEE, vol. 70, NO. 5, May 1982.

35. J. Yang, H. Fang, "Analysis of a Rotating Elastic Beam with Piezoelectric Films as an Angular Rate Sensor," IEEE Transaction on Ultrasonics, Ferroelectrics and Frequency Control, vol. 49, NO. 6, June 2002.

36. C. Acar, A. Shkel, "An approach for Increasing Drive-Mode Bandwidth of MEMS Vibratory Gyroscopes," Journal of Microelectromechanical Systems, vol. 14, NO. 3, June 2005.

37. J. Yang, "A Review of Analyses Related to Vibrations of Rotating Piezoelectric Bodies and Gyroscopes," IEEE Transactions on Ultrasonics and Ferroelectrics and Frequency Control, vol. 52, NO. 5, May 2005.

38. D. Piyabongkarn, R. Rajamani, M. Greminger, "The Development of a MEMS Gyroscope for Absolute Angle Measurement," IEEE Transactions on Control Systems Technology, vol. 13, NO. 2, March 2005.

39. H. Sato, T. Fukuda, F. Arai, K. Itoigawa, Y. Tsukahara, "Parallel-Beam Sensor/Actuator Unit and its Application to the Gyroscope," IEEE/ASME Transactions on Mechatronics, vol. 5, NO. 4, September 2000.

40. A. Katz, A. Highsmith, "The Optimal Size of a Resonant Vibrating Beam Gyroscope," Journal of Dynamic Systems, Measurement, and Control, 2001.

41. J. Bustillo, R. Howe, R. Muller, "Surface Micromachining for Microelectromechanical Systems," Proceed. IEEE, vol. 86, NO. 8, August 1998.

42. L. Dong and R.P. Leland, "The adaptive control system of a MEMS gyroscope with time-varying rotation rate," in Proceedings of the American Control Conference, pp. 3592-3597, 2005.

43. R. Leland, “Lyapunov based adaptive control of a MEMS gyroscope,” in proceedings of American Control Conference, pp.3765-3770, 2002.